Hemodynamic forces tune the arrest, adhesion and extravasation of circulating tumor cells

Gautier Follain[1-4], Naël Osmani[1-4], Sofia Azevedo[1-4], Guillaume Allio[1-4], Luc Mercier[1-4], Matthia A. Karreman[5], Gergely Solecki[6], Nina Fekonja[1-4], Claudia Hille[7], Vincent Chabannes[8], Guillaume Dollé[8], Thibaut Metivet[8], Christophe Prudhomme[8], Bernhard Ruthensteiner[9], André Kemmling[10], Susanne Siemonsen[11], Tanja Schneider[11], Jens Fiehler[11], Markus Glatzel[12], Frank Winkler[6], Yannick Schwab[5], Klaus Pantel[7], Sébastien Harlepp[2,13-14], Jacky G. Goetz[1-4*]

[1]INSERM UMR_S1109, MN3T, Strasbourg, F-67200, France.

[2]Université de Strasbourg, Strasbourg, F-67000, France.

[3]LabEx Medalis, Université de Strasbourg, Strasbourg, F-67000, France.

[4]Fédération de Médecine Translationnelle de Strasbourg (FMTS), Strasbourg, F-67000, France.

[5]Cell Biology and Biophysics Unit, European Molecular Biology Laboratory, Heidelberg, 69117, Germany.

[6]Department of Neurooncology, University Hospital Heidelberg, Heidelberg, 69120, Germany and Clinical Cooperation Unit Neurooncology, German Cancer Research Center (DKFZ), Heidelberg, 69120, Germany.

[7]Institute of Tumor Biology, University Medical Center Hamburg-Eppendorf, Martinistrasse 52, Hamburg, 20246, Germany.

[8]LabEx IRMIA, CEMOSIS, Université de Strasbourg, Strasbourg, F-67000 France.

[9]Zoologische Staatssammlung München, Munich, 81247, Germany.

[10]Department of Neuroradiology, University Medical Center Schleswig-Holstein, Campus Lübeck, 23535 Lübeck, Germany

[11]Department of Diagnostic and Interventional Neuroradiology, University Medical Center Hamburg-Eppendorf, 20246 Hamburg, Germany

[12]Center for Diagnostics, Institute of Neuropathology, University Medical Center Hamburg-Eppendorf, 20246 Hamburg, Germany

[13]CNRS UMR7504, Institut de Physique et Chimie des Matériaux de Strasbourg (IPCMS), Strasbourg, F-67000, France.

[14]LabEx NIE, Université de Strasbourg, Strasbourg, F-67000, France.

Materials and correspondance (*):

Jacky G. GOETZ, jacky.goetz@inserm.fr

INSERM UMR_S1109, The Microenvironmental Niche in Tumorigenesis and Targeted Therapy, 67200 Strasbourg, France; LabEx Medalis, Fédération de Médecine Translationnelle de Strasbourg (FMTS), 67000 Strasbourg, France

Web: www.goetzlab.com, twitter: @GoetzJacky

ABSTRACT

Metastatic seeding is driven by cell-intrinsic and environmental cues, yet the contribution of biomechanics is poorly known. We aim to elucidate the impact of blood flow on the arrest and the extravasation of circulating tumor cells (CTCs) *in vivo*. Using the zebrafish embryo, we show that arrest of CTCs occurs mostly in vessels with favorable flow profiles where flow forces control the adhesion efficacy of CTCs to the endothelium. We biophysically identified the threshold values of flow and adhesion forces allowing successful arrest of CTCs. In addition, flow forces fine-tune tumor cell extravasation by impairing the remodeling properties of the endothelium. Importantly, we also observe endothelial remodeling at arrest sites of CTCs in mouse brain capillaries. Finally, we observed that human supratentorial brain metastases preferably develop in areas with low perfusion. Altogether, these results demonstrate that hemodynamic profiles at metastatic sites regulate key steps of extravasation preceding metastatic outgrowth.

KEYWORDS

Blood flow, extravasation, metastasis, endothelial remodeling, circulating tumor cells, cell adhesion, biomechanics, zebrafish

INTRODUCTION

Metastatic progression is a complex process resulting in the formation of lethal secondary tumors at distance of its origin[1]. Metastatic cancer cells disseminate very efficiently throughout the body upon intravasation in the blood circulation. Recent work on breast cancer suggests that about 80% of metastases originate from early disseminated cancer cells[2,3]. Once in the blood stream, circulating tumor cells (CTCs) may find a location favoring arrest and stable adhesion before extravasating, and avoiding the hostile shear forces[4,5]. After extravasation, metastatic cells either remain dormant[6] or grow successfully into life-threatening secondary tumors[7]. Although multiple mechanisms have been postulated for successful extravasation and outgrowth of metastatic cells[7–10], there are only little informations on the role played by mechanical cues encountered in the blood, the main route for hematogenous metastatic dissemination.

Biomechanical forces are known to have a major impact on tumor progression, leading to metastatic growth. For example, tumor cells sense and respond to stiffening of the surrounding stroma by increasing their invasive potential[11–13]. High extravascular stress caused by tumor growth[14,15] and interstitial fluid pressure[16] leads to vascular compression that impairs perfusion and eventually promotes tumor progression, immunosuppression, and treatment resistance. Locally, invading tumor cells need to overcome physical tissue constraints by cellular and nuclear deformability[17,18], possibly inducing nuclear envelope rupture and DNA damage[19] leading eventually to inheritable genomic instability[20]. Overall, while the impact of biomechanics on tumor growth and invasion are mechanistically relatively well understood, the *in vivo* mechanisms driving arrest, survival and successful extravasation of CTCs, preceding metastatic growth, remain to be elucidated.

Indeed, very little is known about how CTCs arrest and adhere to the endothelium of small capillaries and leave the blood stream by crossing the vascular wall. While the “seed and soil” concept states that metastasis will occur at sites where the local microenvironment is favorable[21], the “mechanical” concept argues that arrest and metastasis of CTC occur at sites of optimal flow patterns[22]. CTCs in the blood circulation are subjected to vascular routing[23], collisions and associations with blood cells[24], hemodynamic shear forces[25] and physical constraints imposed by the vessel architecture[7,9]. Only CTCs capable of overcoming or exploiting the deleterious effects of shear forces will eventually arrest, adhere to and exit the vasculature to form a

secondary tumor[26]. Interestingly, upon arrest in lung microvessels, shear flow disrupts CTCs into microparticles that prime and recruit myeloid cells thereby stimulating successful metastasis from surviving CTC[9]. Nevertheless, a direct contribution of mechanical cues to the arrest and successful extravasation of CTCs has only been poorly studied so far[26]. Therefore, new *in vivo* models, where modeling, visualization and biophysical quantification of the extravasation parameters are easily performed, are of utmost importance for assessing whether biomechanics regulate metastatic extravasation.

Here, we aim to address the direct impact of the blood flow on the arrest and extravasation of CTCs *in vivo*. We developed an original experimental approach to measure and modulate blood flow with intravascular injection of CTCs within zebrafish (ZF) embryos. We observed that blood flow controls the sequential steps of arrest, adhesion and extravasation of CTCs *in vivo*. In parallel, using microfluidics and optical tweezers, we identified the critical adhesion force (80 pN) that CTCs require to initiate adhesion to the endothelium which rapidly stabilizes under shear flow. This value matches the threshold dragging force measured *in vivo* at extravasation sites. Finally, we used our recently-developed intravital correlative light and electronic microscope (CLEM)[27–29], to identify endothelial remodeling as one of the major extravasation mechanisms *in vivo*, and that endothelial remodeling scales with flow velocities. Overall our studies demonstrate that blood flow forces at metastatic sites regulate key steps of extravasation preceding metastatic outgrowth.

RESULTS

Arrest and adhesion of CTC is favored by permissive flow velocities

In order to test the impact of blood flow on the arrest, adhesion and extravasation of CTCs, we experimentally modeled metastatic seeding in endothelium-labeled ZF embryo (*Tg(Fli1a:EGFP)*) at 2 days post-fertilization (dpf) by injecting fluorescently-labeled tumor cells (D2A1 LA-RFP) in the duct of Cuvier (Figure 1A,B). While metastatic extravasation can be successfully tracked in this model[30], the ZF embryo further allows to combine biophysical characterization and manipulation of blood flow parameters with long-lasting and high-resolution imaging of tumor cells *in vivo*. We first quantified and mapped the position of arrested and stably adherent tumor cells in the ZF vasculature and noticed that CTCs preferentially arrested (and extravasated) in the caudal plexus (CP) (Figure 1C). Although arrest and extravasation can be also observed in inter-somitic vessels (ISV) (Figure 1C) and in the brain of ZF embryos (Figure 1C, Figure S1, Movie 1), the majority of the tumor cells arrest in the caudal plexus. We exploited the highly stereotyped vasculature of this region for compiling 20 embryos and quantitatively identifying a major hotspot of arrest in this region (Figure 1D), that sits in between the caudal artery and the venous plexus. Using fast imaging of the blood flow (100 fps) within the entire ZF embryo, combined with PIV (Particle Image Velocimetry) analysis, we observed decreasing flow values in the vascular region that is permissive for the CTC arrest (Figure 1E-F, Movie 2). Accurate dissection of blood flow profiles using PIV analysis showed that flow velocity progressively decreases from the anterior dorsal aorta (Position 1, maximal velocity, v_{max} = 2500 µm/sec, Figure 1E-F), to a minimal flow in its most posterior region (Positions 5 to 6, v_{max} = 500 µm/sec), which we named the arterio-venous junction (AVJ). We have shown in the past that blood flow dissipates along the vascular network of the ZF embryo[31]. In addition, the mass conservation implies that ramification of the vessels in the AVJ further contributes to the blood flow decrease. We thus set out to model this phenomenon *in silico* using mathematical simulation of the blood flow in the CP. To do so, we modelled a simplified geometry of the CP in 3D based on fine 3D confocal microscopy segmentation. Simulation experiments reproduced the flow drop observed in the most posterior region of the CP (Figure S2, Movie 3). Besides, to determine whether flow velocity can impact CTCs arrest, we developed an *in vitro* approach to mimic *in vivo* flow profiles in microfluidic channels previously coated with endothelial cells (EC, Figure 1G). We observed that adhesion

of CTCs to the endothelial layer was favored by low flow profiles (peak velocities of 100 to 400 µm/sec) (Figure 1G), similar to those measured *in vivo* in the AVJ (Figure 1D-E). Using high flow profiles that mimic flow values obtained in the anterior DA prevented efficient adhesion of CTCs to the endothelial layer (Figure 1G), as observed *in vivo* where no adhesion could be observed in the DA between position 1 and 4 (Figure 1D-E). Finally, similar flow profiles were measured in vessels favoring extravasation of CTCs in the ZF brain (Figure S1C, Movie 1). Taken together, these data suggest that low flow profiles are permissive for stable adhesion of CTCs to the endothelium, and that the threshold velocity value for efficient adhesion of CTCs ranges from 400 to 600 µm/sec.

Permissive flow profiles promote stable adhesion of CTCs to the endothelium

Adhesion of CTCs to the endothelium is an important feature that precedes their extravasation[32]. Furthermore, mechanical constraints imposed by cell size and vessel topology likely favor the initial arrest of CTCs[7,33,34]. We set out to test whether such features also contribute to arrest and adhesion in the ZF embryo by accurately measuring both CTC and vessel diameters, with a high-resolution reconstruction of the CP lumen (Movie 4). We measured an average diameter of ~10 µm for the tumor cells (D2A1) in suspension, mimicking CTCs (Figure 2A). We validated this model by comparing this value to average diameters of human CTCs isolated from breast and lung cancer patients (ranging from 7 to 29 µm)(Figure 2A). The diameters of the DA, the AVJ and the caudal vein (CV) each displayed a minimal value of ~15 µm (Figure 2B), suggesting that size limitation is not the main cause for successful arrest of CTCs, when circulating as single cells. This led us to test the role of adhesion molecules in driving successful, flow-dependent, arrest of CTCs. We have observed that intravascular CTCs are capable of efficiently crawling on the vessel wall, suggesting that CTCs establish firm adhesions with the endothelium (Movie 5). In addition, we took advantage of our *in vitro* microfluidic approach and used the optical tweezers (OT) technology to trap and stick CTCs to the EC monolayer. Doing so, we identified an average value of 80 pN for the very early adhesion forces (less than 1 min after adhesion of the CTC to the endothelial layer) required for the attachment of CTCs to ECs (Figure S3A, Movie 6). Interestingly, applying the Stokes law to measure the correspondence between flow and force intensity, we noted that a value of 80 pN represents an average flow value of 450 µm/sec, which agrees with

threshold flow values that we measured both *in vivo* and *in vitro* (Figure 1). Thus, CTCs establish very quickly adhesion forces that allow them to sustain flow velocities of 450 µm/sec.

To test the role of adhesion molecules, we targeted ß1 integrins (ITGB1), known to play a central role in tumor metastasis[35] and promote stable adhesion of CTC to the endothelium before extravasation[36,37]. We determined whether compromising stable adhesion mediated by ß1 integrins would affect the ability of CTC to arrest under permissive flows. We depleted ITGB1 in our cells using a siRNA approach (Figure 2C) and assessed their stable adhesion 3hpi using a heatmapping procedure (see supplementary methods) over several embryos. Interestingly, the adhesion pattern showing an adhesion hotspot in the AVJ is conserved (Figure 2D) but the overall number of adhesion event is significantly reduced (Figure 2E). Similar observations were made in our microfluidic system where only 20% of ITGB1-depleted CTCs stably adhere to the EC monolayer using the same perfusion parameters (Figure 2F). Comparable values were obtained when adhesion (or detachment) of perfused CTCs to (from) ECs was forced using OT in microfluidic channels (Figure S3B, Movie 7) indicating, that permissive flow profiles, combined with proper adhesion forces, allow stable adhesion of CTCs to the endothelium.

To further support this hypothesis, we assessed whether adhesion events could be observed *in vivo* using intravital CLEM[38], which allows to combine live imaging of xenografted CTCs in the ZF embryo with Transmission Electron Microscopy (TEM) and Electron tomography (ET). Interestingly, CTCs that were arrested in the ZF vasculature only 15 mpi displayed finger-like adhesive contacts with endothelial cells (Figure 2G). In addition, ECs displayed long protrusions when in contact with arrested CTCs (upper panels, Figure 2G). These observations suggest that integrin-dependent adhesion forces between early arrested CTCs and ECs are quickly exceeding stripping forces from the blood flow. We aimed to further demonstrate the contribution of early adhesion forces to flow-dependent arrest of CTCs and we performed OT *in vivo.* Although OT can very efficiently trap circulating red blood cells (RBCs) in the vasculature of living ZF embryo (Movie 8) and detach adhered CTCs from ECs *in vitro* (Figure S3B), OT was inefficient for detaching arrested CTCs *in vivo* (Figure 2H, Movie 8). The inability to detach >35 arrested CTCs with OT, demonstrates that early adhesion forces rapidly exceed 200 pN (which is the technical limit of our OT set-up). Altogether, these results suggest that low flow

forces (~80pN) enable the arrest and stable adhesion of CTCs *in vivo*, and ITGB1 mediates stable adhesion (and subsequent increase in adhesion forces) of CTCs to ECs.

Pharmacological tuning of hemodynamic forces modulates pacemaker activity

Since arrest of CTCs occurs at site of permissive flow patterns, we investigated whether tuning flow forces would impact arrest efficacy. We first took advantage of the possibility to tune the ZF pacemaker activity and subsequent flow forces using pharmacological treatments. We selected lidocain[39] and Isobutylmethylxanthine (IBMX)[40] to decrease or increase the pacemaker activity (PMA), respectively (Figure 3A,G). Upon treatment, we assessed cardiac PMA and measured an average decrease and increase of 20% for lidocain and IBMX respectively. Using fast imaging combined with PIV analysis we determined the resulting velocities in 3 positions of the DA for several embryos (ISV 1, 4 and 8) and observed that lowering or increasing PMA with lidocain and IBMX, respectively, significantly altered flow profiles (Figure 3B,H, Movie 9). In brief, while lidocain treatments led to lower velocities with longer times under 400 µm/sec (Fig.3B,S4A), IBMX significantly increased the maximum velocities of flow pulses and decreased the overall duration of the flow under 400 µm/sec (Fig.3H, S4A). We confirmed the impact of the two drugs on flow profiles using *in silico* 3D flow simulation (Fig.S5, Movie 10). We further assessed the impact of tuning PMA on hemodynamic forces by trapping RBCs using OT in the AVJ region *in vivo* (Figure S4B, Movie 11). We measured the forces exerted on trapped RBCs, both at the vessel wall and in its center, and extracted the corresponding flow profile based on the Poiseuille law for each condition (Figure S4B). While lidocain significantly reduced flow forces in the center of the vessel, IBMX increased flow forces at the vessel wall and in the center (Figure 3C,I). Importantly, before taking on experiments aiming to study the behavior of CTCs in distinct flow profiles, we demonstrated that our pharmacological treatments had no impact on the vasculature architecture and permeability (Figure S6A to D, Movie 12), and the migratory and adhesive properties of tumor cells (TCs) *in vitro* (Fig.S6E to G).

Low flow promotes early arrest of CTCs

We then assessed the impact of modulating flow forces on the arrest of CTCs using live and instantaneous intravital imaging upon injection (Figure 3D,J, Movie 13). As

expected, CTCs mostly arrest in the AVJ in normal flow profiles (Figure 3D-E, J-K, Vehicle). Interestingly, decreasing flow profiles with lidocain induced arrest of CTCs in anterior regions of the DA, decreased the number of CTCs in the blood flow over a period of 5 minutes post-injection (mpi) and significantly increased their mean arrest time over the imaging period (Figure 3D-F). In contrast, increasing flow profiles with IBMX drastically abrogated the arrest of CTCs in the blood flow over a period of 5 mpi and reduced their mean arrest time (Figure 3J-L). Altogether, these results show that while low flow forces enhance the arrest probability of CTCs, high flow profiles are capable of impeding their early arrest.

Hemodynamic forces tune the stable intravascular adhesion of CTCs

Because extravasation of CTCs requires stable adhesion to the vessel wall, we investigated whether tuning flow profiles would impact stable adhesion of CTCs to ECs *in vivo*. We first assessed the number and location of arrested CTCs 3 hpi in a large number of embryos, making use of our heatmapping protocol and the stereotyped vasculature of the ZF caudal plexus (Figure 4A, D). While normal flow conditions favored the definitive arrest in the AVJ, decreasing flow forces with lidocain stimulated the stable adhesion of CTCs in more anterior regions of the DA and reduced the proportion of CTCs arresting in the AVJ (Figure 4A-C). On the contrary, increasing flow forces with IBMX impaired the stable arrest in the DA and AVJ regions, and shifted definitive arrest towards venous regions of the caudal plexus (Figure 4D-F). We further consolidated this observation by using two additional drugs known to decrease (nifedipin[41]) and increase (norepinephrine [40]) PMA (Figure S7A,F). Decreasing flow forces with nifedipin favored the arrest of CTCs in more anterior regions of the DA, increasing flow forces with norepinephrine significantly favored the stable adhesion of CTCs in the CV region of the caudal plexus (Figure S7B-C, G-I). Reassuringly, none of these drugs altered the adhesion or migration properties of TCs *in vitro* (Figure S7D-E, H-J). Altogether, these data suggest that flow forces finely tune the adhesive capacity of CTCs, independently of the vessel architecture.

High flow promotes extravasation of CTCs

Once stably attached to the vessel wall, CTCs need to withstand the shear forces and undergo extravasation for metastatic outgrowth. We thus further investigated

whether flow forces could impact the extravasation abilities of arrested CTCs and assessed the location and ratio of extravascular cells 24 hpi. Most of the arrested CTCs eventually undergo extravasation in normal flow conditions, while impairing flow forces with lidocain drastically reduced the number of extravascular cells. More than 60% of cells remained fully intravascular, in particular along anterior regions of the DA where CTCs mostly arrested in low flow conditions (Figure 5A-B). Using our CLEM protocol, we confirmed that the TCs were extravascular in normal flow conditions using serial TEM (Figure 5E, Movie 14). Similar experiments conducted on lidocain-treated embryos showed that the vast majority of the cells remain indeed fully intravascular (Figure 5E). In contrast, increasing flow forces with IBMX further increased the ratio of extravascular cells (close to 100%) (Figure 5C-D), and favored the formation of micrometastasis foci that were surrounded by the local vasculature, as depicted in the 3D view (Figure 5C). Overall, these results show that blood flow forces enhance the extravasation abilities of CTCs.

Flow-dependent endothelial remodeling drives extravasation of CTCs

We noticed that ECs could react very quickly to the presence of arrested CTCs (Figure 2G) and that extravasation of CTCs induces massive remodeling of the local vasculature (Figure 5C). In addition, our drugs had no effect on the behavior of the TCs (Figure S6-7), which prompted us to investigate whether flow forces could impact extravasation via ECs. We thus set up long-lasting (15h) intravital recordings of the behavior of arrested CTCs during extravasation using 3D confocal microscopy (Figure 6A, Movie 15). Unexpectedly, image analysis revealed that a majority of CTCs extravasated by indoctrinating the local vasculature rather than by actively transmigrating through the vessel wall by diapedesis, which is nevertheless also observed (Figure 6B-D). Indeed, ECs actively remodeled around the arrested CTCs by slowly protruding and establishing tight connections with other ECs. During this process, endothelial cells progressively engulf single or cluster of arrested CTCs, allowing full reperfusion of the vessel while inducing extravasation of CTCs. In order to gain further structural insights into this phenomenon, we took advantage of our intravital CLEM procedure on ZF embryos only 9 hpi, which allows us to dissect the behavior of CTCs and associated ECs that are engaged in extravasation (Figure 6E). 3D TEM analysis revealed that clusters of arrested CTCs are indeed fully surrounded by ECs (Figure 6F-G, Movie 16). High-resolution images performed via ET (Electron

Tomography) showed that ECs could establish tight contact around the cluster of arrested CTCs (Figure 6H), suggesting that ECs are also actively participating to the extravasation of CTCs.

We further examined embryos 3, 9 and 24 hpi and documented the behavior of the associated ECs (pocketing) over a high number of arrested CTCs (Figure 6I), over time, and in dependence of the blood flow profiles. Interestingly, impairing flow forces *in vivo* with lidocain significantly impaired the ability of ECs to engage pocketing over arrested CTCs (Figure 6J-K) suggesting that blood flow is essential for maintaining the remodeling ability of the endothelium. Remarkably, in normal flow conditions, injected CTCs that are fully intravascular are rapidly (≈3hpi) accompanied by a massive EC pocketing that drives successful extravasation of TCs (Figure 6J). On the contrary, low flow significantly delays the pocketing behavior of ECs (≈9hpi) impairing efficient extravasation of intravascular TCs (Figure 6K). We then wondered whether this flow-dependent phenomenon could be reproduced *in vitro* and set out a microfluidic experiment where CTCs were perfused over a monolayer of ECs for 10 minutes and incubate 16h under perfusion (or not) before assessing the behavior of ECs. We observed that flow stimulated the transmigration of TCs. Interestingly, TCs that transmigrated through the HUVECs monolayer were mostly engulfed by ECs, mimicking the pocketing phenomenon we had observed *in vivo* (Figure 6L-M). As a consequence, TCs that successfully transmigrated in absence of flow were rarely surrounded by ECs suggesting that they crossed the monolayer by diapedesis. Altogether, these results demonstrate that the extravasation of CTCs occurs via indoctrination of the associated endothelium, and that flow forces are essential for maintaining the remodeling abilities of the vasculature.

Micrometastasis develop from mouse brain capillaries with low flow profiles

We next investigated whether blood flow forces could explain the location of successful extravasation and micrometastasis formation in another model, the mouse brain. We used our intravital imaging set-up[7] to quantify the vascular arrest, extravasation, and successful growth vs. regression in the mouse brain over weeks after intra-cardiac injection of highly metastatic tumor cells (Figure 7A). By analyzing >5000 arrested tumor cells from four different cell lines (JIMT1br3, A2058br, PC14PE6br, H1), we discovered that tumor cells that successfully mastered all step of brain metastatic cascade in microvessels of a specific diameter, shape and depth

(Figure 7B). Next, we measured the associated blood flow velocities of these vessels, and compared them to flow velocities within blood vessels where arrest and extravasation of CTCs never occurred (Figure 7B). Strikingly, the mean flow velocity in metastasis-proficient vessels was 628±46 µm/sec, which is very close to the permissive flow values we had identified in the ZF embryo. In contrast, mean flow velocity of metastasis-deficient vessels was much higher (5880±716 µm/sec). Together, this data suggests that flow-mediated arrest of CTCs could be a universal determinant of tumor metastasis.

Similar to the ZF embryo experiments, we took advantage of our intravital CLEM procedure[28,29] and investigated whether ECs were also influenced by arrested CTCs in the mouse brain. We thus conducted intracardiac injections of Jimt1 cells and recorded the position of arrested CTCs only 3 dpi, where most of the CTCs are still intravascular (Figure 7C). Our workflow driven by X-ray micro-computed tomography (mCT) allowed us to successfully retrieve arrested CTCs in the vasculature of the mouse brain. This enabled us to document, using serial section TEM, the ultrastructure of the arrested TC (Figure 7C-D), of its associated vessel (Figure 7C-D) and of neighboring vessels where no CTC could be observed (Figure 7C,E). Blood vessels where no arrested CTC could be observed displayed a smooth vascular wall (Figure 7E). However, ECs from the vessel containing an arrested CTC displayed a remodeling phenotype, possibly in response to the presence of the arrested cell (Figure 7D). Indeed, multiple endothelial cells could be observed protruding within the vessel lumen, establishing contacts with other cells of the vessel wall and enwrapping the arrested tumor cell while maintaining a lumenized vessel. Altogether, these results obtained in the context of brain metastasis in the mouse suggest that permissive flow profile is a very relevant mechanism driving the arrest of CTCs, leading to successful micrometastasis growth. In addition, the observation of early vascular remodeling in the presence of arrested CTCs further suggest an active reaction of the endothelium to arrested cancer cells during the brain metastatic cascade, which could speak for mechanisms similar to what we have observed in zebrafish.

Blood perfusion controls the location of human brain metastasis (BM)

We next investigated whether blood flow perfusion would control the location of BM in humans. For this purpose, we analyzed a randomly selected cohort of 100 patients

with BM (n=580) in the supratentorial region of the brain (Fig.8A). The BM of each patient were segmented on contrast-enhanced T1-weighted imaging and the sum mask of all patients (Fig.8B) was co-registered with a computed tomography perfusion atlas of a healthy cohort (Fig.8C). We then performed a voxel-wise comparison of regions containing BM (BM+) and those who did not (BM-) (Fig.8D). Strikingly, BM preferably develop in regions with lower cerebral blood flow (CBF, 51±36-61 vs 58±41-76 ml/100g/min, $p<0.001$) and higher mean transit time (MTT, 4.6±4.3-5.1 vs 4.5±4.2-5.0 seconds, $p<0.001$) (Fig.8C,D). These results indicated that occurrence of BM is favored in brain regions with low perfusion, further demonstrating that blood flow patterns are key determinants of metastatic outgrowth.

DISCUSSION

In this work, we have unraveled for the first time the contribution of flow forces *in vivo* on mediating arrest, adhesion and successful extravasation of CTCs, preceding metastatic outgrowth. Using the multiple advantages of the ZF embryo, we have identified a threshold of hemodynamic profiles (400-600 µm/s) that allows stable arrest of CTCs in permissive vascular regions, a prerequisite for metastasis formation (Fig.8E). These values were further confirmed *in vitro* and *in silico* using a combination of microfluidic and 3D flow simulation approaches, which were developed upon accurate *in vivo* measurements of hemodynamic forces. We have shown that these permissive flow profiles promote the formation of transient protrusions establishing integrin-dependent adhesion of CTCs to the endothelium. This fast and weak adhesion is then quickly stabilized (less than a minute *in vitro*) to reach adhesion forces exceeding the shear forces generated by such permissive flow values. This process is impaired in regions with high shear values, where forces are significantly higher than the initial adhesion forces CTCs are able to produce. Reduced or low flow forces favor arrest and metastasis in the zebrafish embryo, but also in mouse brain capillaries. Importantly, we made similar observations in humans where a significant reduction of blood perfusion is observed in pro-metastatic brain regions. Thus, low or reduced flow profiles favor the stable arrest of CTCs preceding metastatic outgrowth (Fig.8E). Once arrest of CTCs within blood vessels is consolidated (through integrins), arrested TCs engage in a second step where blood flow remains essential. Indeed, we have observed that blood flow is required to stimulate endothelial remodeling and subsequent pro-metastatic extravasation. However, although low flow allows arrest of CTCs, it impedes the remodeling potential of ECs, and significantly impairs extravasation of arrested TCs. Thus, pro-metastatic vascular regions are characterized by intermediate flow profiles that are sufficiently low (or reduced) to favor the arrest of CTCs, and sufficiently high to stimulate endothelial remodeling, which could be a fundamental mechanism driving metastasis formation.

While much attention has been given to the contribution of biomechanics to tumor growth and tumor invasion[26,42], only few evidence suggest that biomechanics could also modulate one of the most important steps of tumor progression, namely extravasation and metastatic outgrowth. However, CTCs are shed in the blood

circulation and must survive in a very hostile environment, such as blood shear forces that could induce cell cycle arrest[25] or even necrotic cell death[5]. In addition, CTCs frequently collide with other components of the blood and the vascular wall, reaching capillary-like vascular regions that appear often occlusive[7,9,36]. Size-mediated arrest of CTCs in capillaries occurs in multiple organs such as the lung, the liver and the brain[43]. Moreover, cellular and nuclear rigidity[18] and integrity[19,20] was recently shown to be key drivers of tumor invasion and metastasis. Our work suggests that, in addition to physical occlusion, permissive flows are sufficient to facilitate arrest of CTCs. In the ZF embryo, 50% of arrested TCs did so in vascular regions where diameter of the vessel exceeds diameter of TCs, excluding occlusion mechanisms. In addition, full occlusion of mouse brain capillaries is rarely observed suggesting that blood flow or physical constraints, although they could impact synergistically, are sufficient to promote the arrest of CTCs, preceding metastatic outgrowth. Further work is required to investigate the mutual contribution of cell stiffness/size and the blood flow as determinant factors in arrest and extravasation of CTCs. Interestingly, recent work demonstrates that clusters of CTCs, whose arrest would be favored by physical occlusion, are more potent in driving tumor metastasis[44–46]. Besides, we frequently observed a remarkable behavior of arrested CTCs that do not occlude the blood vessel: they stably crawl counter-flow along the endothelium in fully perfused vessels and tend to cluster intravascularly before extravasating (Movie 5). This process occurs without compromising blood flow and suggests that TCs establish cell-cell contact that could favor successful extravasation.

A fundamental observation made in our study is that low blood flow favors arrest of CTCs in any species (ZF, mouse and human), preceding metastatic outgrowth. Indeed, we first identified a threshold flow velocity value of 400-600 µm/s that favors the arrest of CTCs in the vasculature of the ZF embryo. Using intravital imaging and flow profiling in the mouse brain, we further confirmed that brain capillaries perfused with low flow velocities (around 600 µm/s) are favorable to extravasation and outgrowth of TCs. Finally, we analyzed a cohort of 100 patients with brain metastasis and observed that they preferably develop in regions with lower cerebral blood perfusion. Altogether, these results obtained in various organisms indicate that occurrence of metastasis is favored in vascular regions with reduced perfusion, further demonstrating that blood flow patterns are key determinants of metastatic

outgrowth in the brain. Interestingly, human brain metastasis had been shown to occur preferentially in vascular border zones as well as in the gray and white matter junction[47]. These regions are located at the most distal part of the arterial tree and display sudden drops in vessel diameter, blood pressure and blood flow, making them very susceptible to infarction and ischemia. Our results further demonstrate that such vascular networks are favorable environments for metastatic extravasation.

Another key observation from our work is that low flow promotes arrest of CTCs, by favoring the establishment of intravascular TC-EC adhesions. Indeed, successful arrest of CTCs can be observed in anterior regions of the DA, when flow values are decreased and depletion of ITGB1 drastically impedes the successful arrest of CTCs. We identified an initial TC-EC adhesion force of 80 pN, likely mediated by a few integrin molecules. While ITBGB1 favors TC protrusion into the subendothelial matrix thereby favoring metastatic outgrowth[48], integrin-mediated arrest of CTCs could be favored by interaction between ITGB1 and endothelial adhesion molecules, or extracellular matrix molecules localized on the luminal side of the vascular wall. Indeed, *in vitro* data suggest that CTCs hijack the leukocyte adhesion machinery and arrest using $\alpha 4\beta 1$ integrins to bind the VCAM-1 receptor present at the surface of endothelial cells[49]. Furthermore, *in vivo* imaging of liver metastasis has demonstrated that although lumen occlusion by CTCs is rather frequent, it does not account fully for the efficient extravasation as blocking adhesion with ITGB1-blocking antibody significantly impaired stable cell arrest of CTCs[36]. CTCs can escape mechanical entrapment in the lungs[50] and adhesion-mediated arrest of CTCs has been observed without signs of mechanical entrapment[51]. This suggests that although capillary size can stop CTCs, active adhesion between CTCs and the vascular wall is required for efficient extravasation, and subsequent metastasis. Even if we have not directly visualized this in our experiments, we cannot exclude the CTCs undergo rolling, that could activate ITGB1, before stably arresting. Further work will be required to investigate whether arrest of CTCs follows rules that are commonly used by immune cells before extravasation.

Another important observation of our work is the route used by arrested CTCs to undergo extravasation. Indeed, in most of the cases, extravasation of CTCs engages massive endothelial remodeling, which encapsulate single or clusters of arrested CTCs. This phenomenon has been observed during extravasation of neutrophils and allows the vessel to reduce vascular permeability[52]. We observed that pocketing or

encapsulation of arrested CTCs occurs by the formation of endothelial domes, reminiscent of the ones observed for extravasation of neutrophils[53], that are tightly connected through EC-EC junctions (Figure 6). Recent work performed in ZF embryos has shown that stem cells use similar mechanisms to undergo extravasation[54]. Interestingly, using our intravital CLEM technology, we observed that vascular regions of arrested TCs in the mouse brain also engage massive endothelial remodeling in vessels with permissive flow profiles, suggesting it could drive successful extravasation of brain metastatic cells. Altogether, this reinforces the view that CTCs require a very active contribution of the endothelium to perform successful transmigration of the vascular wall, and challenge the classical idea that CTCs mostly use diapedesis for successful extravasation[55–57]. Along this line, arrested CTCs have been observed to proliferate attached to the luminal wall of lung blood vessels, leading to intraluminal metastatic foci that eventually passively rupture the endothelial barrier[58]. Recent work suggest that arrested CTCs are also capable of driving TC-mediated necroptosis of EC and subsequent metastasis[10], further suggesting that the vascular wall is a key contributor to efficient metastatic outgrowth. While endothelium remodeling of arrested CTCs had been observed *in vivo* in the past[30,59], its importance during metastatic extravasation is still not fully appreciated[60]. We now provide evidence that blood flow actively regulates endothelial remodeling thus promoting successful extravasation. Indeed, both *in vivo* pocketing and *in vitro* endothelial dome formation are increased by flow. As blood flow is known to be key regulator of vascular homeostasis[61,62] and angiogenesis[38,63], it is likely that it is required during extravasation by maintaining its remodeling behavior.

In conclusion, we provide the first *in vivo* demonstration that blood flow, which carries tumor-shed CTCs, actively participates in both CTC stable arrest and extravasation, preceding metastatic outgrowth. Our work identified pro-metastatic vascular regions that are characterized by intermediate flow profiles which are sufficiently low (or reduced) to favor the arrest of CTCs, and sufficiently high to stimulate endothelial remodeling. From our *in vivo* observations, this latter mechanism is fundamental in driving metastasis formation. Our current work aims to identify the molecular mechanisms that are driven by blood flow to successfully encapsulate arrested CTCs. Altogether, this work suggests that therapies that target endothelial remodeling might be useful to impede extravasation, and subsequent outgrowth, of metastatic cells.

AUTHOR CONTRIBUTIONS

G.F. performed most of the experiments and analysis, and wrote the paper. N.O. performed the siITGB1 experiments and analysis, and contributed to Fig.3 and Fig.6. S.A. initiated the project, and performed experiments and analysis. G.A. developed the heatmapping protocol and contributed to blood flow analysis, as well as processing of EM images. L.M. participated to the mouse experiments. M.K. and Y.S. performed EM of the mouse brain metastasis. G.S. and F.W. performed 2PEM imaging of the mouse brain metastasis. C.H. and K.P. isolated and characterized human CTCs. N.F. performed EM in the ZF embryo. V.C, G.D., T.M. and C.P. developed the flow simulation with input from G.F., S.H. and J.G. B.R. and M.K. performed mCT experiments. A.K., S.S., T.S., J.F and K.P. analyzed human brain metastases and blood perfusion patterns on imaging. S.H. supervised the study, performed OT experiments and analysis. J.G. conceived the project, supervised the study, performed experiments and analysis, and wrote the paper with input from G.F., S.H., and N.O.

ACKNOWLEDGMENTS

We thank all members of the Goetz Lab for helpful discussions, in particular to Olivier LEFEBVRE for help with statistical analysis. We are grateful to Tsukasa SHIBUE (MIT) and Bob WEINBERG (MIT) for providing D2A1 cells. We are very much grateful to Francesca PERI (EMBL) and Kerstin RICHTER (EMBL) for providing zebrafish embryos. We thank Anita MICHEL (INSERM U949) and Fabienne PROAMER (INSERM U949) from EFS imaging facility for electronic microscopy. We thank Yohan GERBER for help with the Nifedipin and Norepinephrine experiments. We thank Mourad ISMAIL for the fruitful discussions on flow simulation and Marie HOUILLON for participating to the simulation set up. We thank Martin SCHROB (EMBL) for assistance with Electron Tomography. We thank Gertraud OREND, Vincent HYENNE and Michaël POIRIER for critical reading of the manuscript. This work has been funded by Plan Cancer (OptoMetaTrap, to J.G.. and S.H) and CNRS IMAG'IN (to S.H., J.G. and C.P.) and by institutional funds from INSERM and University of Strasbourg. C.P and V.C were supported by the Center of Modeling and Simulation of Strasbourg (CEMOSIS), ANR MONU-Vivabrain and the Labex IRMIA. G.F. is supported by La Ligue Contre le Cancer. N.O is supported by Plan Cancer. L.M. is supported by an INSERM/Région Alsace Ph.D fellowship. S.A. and G.A. are supported by FRM (Fondation pour la Recherche Médicale). M.A.K. is supported by an EMBL Interdisciplinary Post-doctoral fellowship (EIPOD) under Marie Curie Actions (COFUND).

REFERENCES

1. Nguyen, D. X., Bos, P. D. & Massagué, J. Metastasis: from dissemination to organ-specific colonization. *Nat. Rev. Cancer* **9,** 274–284 (2009).
2. Hosseini, H. *et al.* Early dissemination seeds metastasis in breast cancer. *Nature* (2016). doi:10.1038/nature20785
3. Harper, K. L. *et al.* Mechanism of early dissemination and metastasis in Her2(+) mammary cancer. *Nature* (2016). doi:10.1038/nature20609
4. Valastyan, S. & Weinberg, R. A. Tumor Metastasis: Molecular Insights and Evolving Paradigms. *Cell* **147,** 275–292 (2011).
5. Regmi, S., Fu, A. & Luo, K. Q. High Shear Stresses under Exercise Condition Destroy Circulating Tumor Cells in a Microfluidic System. *Scientific Reports* **7,** 39975 (2017).
6. Sosa, M. S., Bragado, P. & Aguirre-Ghiso, J. A. Mechanisms of disseminated cancer cell dormancy: an awakening field. *Nat. Rev. Cancer* **14,** 611–622 (2014).
7. Kienast, Y. *et al.* Real-time imaging reveals the single steps of brain metastasis formation. *Nat. Med.* **16,** 116–122 (2010).
8. Chen, Q. *et al.* Carcinoma-astrocyte gap junctions promote brain metastasis by cGAMP transfer. *Nature* **533,** 493–498 (2016).
9. Headley, M. B. *et al.* Visualization of immediate immune responses to pioneer metastatic cells in the lung. *Nature* **531,** 513–517 (2016).
10. Strilic, B. *et al.* Tumour-cell-induced endothelial cell necroptosis via death receptor 6 promotes metastasis. *Nature* **536,** 215–218 (2016).
11. Paszek, M. J. *et al.* Tensional homeostasis and the malignant phenotype. *Cancer Cell* **8,** 241–254 (2005).
12. Levental, K. R. *et al.* Matrix crosslinking forces tumor progression by enhancing integrin signaling. *Cell* **139,** 891–906 (2009).
13. Mouw, J. K. *et al.* Tissue mechanics modulate microRNA-dependent PTEN expression to regulate malignant progression. *Nat. Med.* **20,** 360–367 (2014).
14. Stylianopoulos, T. *et al.* Causes, consequences, and remedies for growth-induced solid stress in murine and human tumors. *Proc. Natl. Acad. Sci. U.S.A.* **109,** 15101–15108 (2012).
15. Chauhan, V. P. *et al.* Angiotensin inhibition enhances drug delivery and potentiates chemotherapy by decompressing tumour blood vessels. *Nat Commun* **4,** 2516 (2013).
16. Provenzano, P. P. *et al.* Enzymatic targeting of the stroma ablates physical barriers to treatment of pancreatic ductal adenocarcinoma. *Cancer Cell* **21,** 418–429 (2012).
17. Wolf, K. *et al.* Physical limits of cell migration: control by ECM space and nuclear deformation and tuning by proteolysis and traction force. *J. Cell Biol.* **201,** 1069–1084 (2013).
18. Harada, T. *et al.* Nuclear lamin stiffness is a barrier to 3D migration, but softness can limit survival. *J. Cell Biol.* **204,** 669–682 (2014).
19. Denais, C. M. *et al.* Nuclear envelope rupture and repair during cancer cell migration. *Science* **352,** 353–358 (2016).
20. Irianto, J. *et al.* DNA Damage Follows Repair Factor Depletion and Portends Genome Variation in Cancer Cells after Pore Migration. *Curr. Biol.* (2016). doi:10.1016/j.cub.2016.11.049
21. Paget, S. The distribution of secondary growths in cancer of the breast. 1889. *Cancer Metastasis Rev.* **8,** 98–101 (1989).
22. Weiss, L. Comments on hematogenous metastatic patterns in humans as

revealed by autopsy. *Clin. Exp. Metastasis* **10,** 191–199 (1992).
23. Chambers, A. F., Groom, A. C. & MacDonald, I. C. Dissemination and growth of cancer cells in metastatic sites. *Nat. Rev. Cancer* **2,** 563–572 (2002).
24. Labelle, M., Begum, S. & Hynes, R. O. Platelets guide the formation of early metastatic niches. *Proc. Natl. Acad. Sci. U.S.A.* **111,** E3053–3061 (2014).
25. Chang, S.-F. *et al.* Tumor cell cycle arrest induced by shear stress: Roles of integrins and Smad. *PNAS* **105,** 3927–3932 (2008).
26. Wirtz, D., Konstantopoulos, K. & Searson, P. C. The physics of cancer: the role of physical interactions and mechanical forces in metastasis. *Nat. Rev. Cancer* **11,** 512–522 (2011).
27. Follain, G., Mercier, L., Osmani, N., Harlepp, S. & Goetz, J. G. Seeing is believing – multi-scale spatio-temporal imaging towards in vivo cell biology. *J Cell Sci* **130,** 23–38 (2017).
28. Karreman, M. A., Hyenne, V., Schwab, Y. & Goetz, J. G. Intravital Correlative Microscopy: Imaging Life at the Nanoscale. *Trends Cell Biol.* **26,** 848–863 (2016).
29. Karreman, M. A. *et al.* Fast and precise targeting of single tumor cells in vivo by multimodal correlative microscopy. *J Cell Sci* **129,** 444–456 (2016).
30. Stoletov, K. *et al.* Visualizing extravasation dynamics of metastatic tumor cells. *J Cell Sci* **123,** 2332–2341 (2010).
31. Anton, H. *et al.* Pulse propagation by a capacitive mechanism drives embryonic blood flow. *Development* **140,** 4426–4434 (2013).
32. Reymond, N., d'Água, B. B. & Ridley, A. J. Crossing the endothelial barrier during metastasis. *Nat. Rev. Cancer* **13,** 858–870 (2013).
33. Cameron, M. D. *et al.* Temporal progression of metastasis in lung: cell survival, dormancy, and location dependence of metastatic inefficiency. *Cancer research* **60,** 2541–2546 (2000).
34. Luzzi, K. J. *et al.* Multistep nature of metastatic inefficiency: dormancy of solitary cells after successful extravasation and limited survival of early micrometastases. *The American journal of pathology* **153,** 865–873 (1998).
35. Seguin, L., Desgrosellier, J. S., Weis, S. M. & Cheresh, D. A. Integrins and cancer: regulators of cancer stemness, metastasis, and drug resistance. *Trends Cell Biol.* **25,** 234–240 (2015).
36. Gassmann, P., Hemping-Bovenkerk, A., Mees, S. T. & Haier, J. Metastatic tumor cell arrest in the liver–lumen occlusion and specific adhesion are not exclusive. *International Journal of Colorectal Disease* **24,** 851–858 (2009).
37. Schlesinger, M. & Bendas, G. Contribution of very late antigen-4 (VLA-4) integrin to cancer progression and metastasis. *Cancer Metastasis Rev.* **34,** 575–591 (2015).
38. Goetz, J. G. *et al.* Endothelial Cilia Mediate Low Flow Sensing during Zebrafish Vascular Development. *Cell Reports* **6,** 799–808 (2014).
39. Vermot, J. *et al.* Reversing blood flows act through klf2a to ensure normal valvulogenesis in the developing heart. *PLoS Biol.* **7,** e1000246 (2009).
40. Luca, E. D. *et al.* ZebraBeat: a flexible platform for the analysis of the cardiac rate in zebrafish embryos. *Scientific Reports* **4,** 4898 (2014).
41. Brennan, C. Acetylcholine and calcium signalling regulates muscle fibre formation in the zebrafish embryo. *Journal of Cell Science* **118,** 5181–5190 (2005).
42. Kai, F., Laklai, H. & Weaver, V. M. Force Matters: Biomechanical Regulation of Cell Invasion and Migration in Disease. *Trends Cell Biol.* **26,** 486–497 (2016).
43. Azevedo, A. S., Follain, G., Patthabhiraman, S., Harlepp, S. & Goetz, J. G. Metastasis of circulating tumor cells: favorable soil or suitable biomechanics, or

both? *Cell Adh Migr* **9,** 345–356 (2015).
44. Cheung, K. J. & Ewald, A. J. A collective route to metastasis: Seeding by tumor cell clusters. *Science* **352,** 167–169 (2016).
45. Cheung, K. J. *et al.* Polyclonal breast cancer metastases arise from collective dissemination of keratin 14-expressing tumor cell clusters. *Proc. Natl. Acad. Sci. U.S.A.* **113,** E854–863 (2016).
46. Aceto, N. *et al.* Circulating tumor cell clusters are oligoclonal precursors of breast cancer metastasis. *Cell* **158,** 1110–1122 (2014).
47. Hwang, T. L., Close, T. P., Grego, J. M., Brannon, W. L. & Gonzales, F. Predilection of brain metastasis in gray and white matter junction and vascular border zones. *Cancer* **77,** 1551–1555 (1996).
48. Chen, M. B., Lamar, J. M., Li, R., Hynes, R. O. & Kamm, R. D. Elucidation of the Roles of Tumor Integrin β1 in the Extravasation Stage of the Metastasis Cascade. *Cancer Res.* **76,** 2513–2524 (2016).
49. Klemke, M., Weschenfelder, T., Konstandin, M. H. & Samstag, Y. High affinity interaction of integrin alpha4beta1 (VLA-4) and vascular cell adhesion molecule 1 (VCAM-1) enhances migration of human melanoma cells across activated endothelial cell layers. *J. Cell. Physiol.* **212,** 368–374 (2007).
50. Glinskii, O. V. *et al.* Mechanical entrapment is insufficient and intercellular adhesion is essential for metastatic cell arrest in distant organs. *Neoplasia* **7,** 522–527 (2005).
51. Enns, A. *et al.* Integrins can directly mediate metastatic tumor cell adhesion within the liver sinusoids. *J. Gastrointest. Surg.* **8,** 1049–1059; discussion 1060 (2004).
52. Petri, B. *et al.* Endothelial LSP1 is involved in endothelial dome formation, minimizing vascular permeability changes during neutrophil transmigration in vivo. *Blood* **117,** 942–952 (2011).
53. Phillipson, M., Kaur, J., Colarusso, P., Ballantyne, C. M. & Kubes, P. Endothelial domes encapsulate adherent neutrophils and minimize increases in vascular permeability in paracellular and transcellular emigration. *PLoS ONE* **3,** e1649 (2008).
54. Allen, T. A. *et al.* Angiopellosis as an Alternative Mechanism of Cell Extravasation. *Stem Cells* **35,** 170–180 (2017).
55. Heyder, C. *et al.* Realtime visualization of tumor cell/endothelial cell interactions during transmigration across the endothelial barrier. *J. Cancer Res. Clin. Oncol.* **128,** 533–538 (2002).
56. Khuon, S. *et al.* Myosin light chain kinase mediates transcellular intravasation of breast cancer cells through the underlying endothelial cells: a three-dimensional FRET study. *J Cell Sci* **123,** 431–440 (2010).
57. Tremblay, P.-L., Huot, J. & Auger, F. A. Mechanisms by which E-selectin regulates diapedesis of colon cancer cells under flow conditions. *Cancer Res.* **68,** 5167–5176 (2008).
58. Al-Mehdi, A. B. *et al.* Intravascular origin of metastasis from the proliferation of endothelium-attached tumor cells: a new model for metastasis. *Nat Med* **6,** 100–102 (2000).
59. Lapis, K., Paku, S. & Liotta, L. A. Endothelialization of embolized tumor cells during metastasis formation. *Clinical & experimental metastasis* **6,** 73–89 (1988).
60. Lambert, A. W., Pattabiraman, D. R. & Weinberg, R. A. Emerging Biological Principles of Metastasis. *Cell* **168,** 670–691 (2017).
61. Franco, C. A. *et al.* Dynamic endothelial cell rearrangements drive developmental vessel regression. *PLoS Biol.* **13,** e1002125 (2015).

62. Gebala, V., Collins, R., Geudens, I., Phng, L.-K. & Gerhardt, H. Blood flow drives lumen formation by inverse membrane blebbing during angiogenesis in vivo. *Nat. Cell Biol.* **18,** 443–450 (2016).
63. Potente, M., Gerhardt, H. & Carmeliet, P. Basic and therapeutic aspects of angiogenesis. *Cell* **146,** 873–887 (2011).
64. Shibue, T., Brooks, M. W. & Weinberg, R. A. An integrin-linked machinery of cytoskeletal regulation that enables experimental tumor initiation and metastatic colonization. *Cancer Cell* **24,** 481–498 (2013).
65. Osswald, M. *et al.* Brain tumour cells interconnect to a functional and resistant network. *Nature* **528,** 93–98 (2015).
66. Prud'Homme, C. *et al.* Feel++: A Computational Framework for Galerkin Methods and Advanced Numerical Methods. *ESAIM: Proceedings* **38,** 429–455 (2012).
67. Burman, E. & Fernández, M. A. Explicit strategies for incompressible fluid-structure interaction problems: Nitsche type mortaring versus Robin-Robin coupling. *International Journal for Numerical Methods in Engineering* **97,** 739–758 (2014).
68. Hvichia, G. E. *et al.* A novel microfluidic platform for size and deformability based separation and the subsequent molecular characterization of viable circulating tumor cells. *Int. J. Cancer* **138,** 2894–2904 (2016).
69. Chudziak, J. *et al.* Clinical evaluation of a novel microfluidic device for epitope-independent enrichment of circulating tumour cells in patients with small cell lung cancer. *Analyst* **141,** 669–678 (2016).
70. Magbanua, M. J. M. *et al.* A Novel Strategy for Detection and Enumeration of Circulating Rare Cell Populations in Metastatic Cancer Patients Using Automated Microfluidic Filtration and Multiplex Immunoassay. *PLoS ONE* **10,** e0141166 (2015).
71. Robb, R. A. The biomedical imaging resource at Mayo Clinic. *IEEE Trans Med Imaging* **20,** 854–867 (2001).
72. Nudelman, K. N. H. *et al.* Altered cerebral blood flow one month after systemic chemotherapy for breast cancer: a prospective study using pulsed arterial spin labeling MRI perfusion. *PLoS ONE* **9,** e96713 (2014).
73. Schwarzbach, C. J. *et al.* Stroke and cancer: the importance of cancer-associated hypercoagulation as a possible stroke etiology. *Stroke* **43,** 3029–3034 (2012).
74. Feyen, L. *et al.* Standardization of Dynamic Whole-Brain Perfusion CT: A Comprehensive Database of Regional Perfusion Parameters. 189–220 (2010).
75. Abels, B., Klotz, E., Tomandl, B. F., Kloska, S. P. & Lell, M. M. Perfusion CT in Acute Ischemic Stroke: A Qualitative and Quantitative Comparison of Deconvolution and Maximum Slope Approach. *American Journal of Neuroradiology* **31,** 1690–1698 (2010).
76. Kemmling, A. *et al.* Decomposing the Hounsfield unit: probabilistic segmentation of brain tissue in computed tomography. *Clin Neuroradiol* **22,** 79–91 (2012).

FIGURE LEGENDS

Figure 1: Arrest and stable adhesion of CTCs are favored by permissive blood flow profiles in the ZF embryo. (A-B) Experimental design and workflow. xpi: minutes or hours post-injection. (C) Representative images (*Head, head region; CP,* Caudal Plexus) and quantification of arrested CTCs (red) in the vasculature (green) of the ZF embryo at 3 hpi (See also Movie 1). Ant., Mid and Post.: Anterior, mid and posterior plexus as depicted in D. (D) High-magnification image of the vascular caudal plexus, the associated regions, and heatmap of arrested CTCs at 3 hpi (n=20 embryos). *AVJ*: arterio-venous junction. *DA*: Dorsal aorta. *CV*: Caudal veins. Arrows indicate blood flow direction. (E) Blood flow velocity measurements (PIV) in the indicated region (red and blue squares 1 to 8) of the ZF embryo. Arrows indicate blood flow direction (See also Movies 2&3). (F) Minimum, maximum and mean values of the blood flow velocity are plotted over the 8 different regions (n=3 embryos). (G) Experimental set-up, representative images and quantification of the microfluidic approach. CTCs (green) are perfused over a monolayer of HUVECs (ECs, red) and adhesion is quantified (n=5 to 6 independent channel per conditions). Pulsatile flow corresponds to 0.3 sec perfusion/0.3 sec stop of the peristatique pump. Values in (C), (E), (F) and (G) are mean ±SD (gray area in E). *p <0,05, **p < 0.01, ***p <0.001. Kruskal-Wallis test and Dunn's multiple comparisons post-test.

Figure 2: Arrest of CTCs depends on early cellular adhesion forces. (A) Quantification of the diameters of human CTCs (gray, five breast cancer patients and one lung cancer patient) and D2A1 cells (red) in suspension (number of cells quantified is provided). Representative images of D2A1 and of human CTCs are also provided. Human CTCs are labeled with Pan-Keratin (CTC marker), CD45 and DAPI (nucleus). Red dotted line shows the mean diameter of D2A1 cells. (B) Representative confocal Z-projection image of the caudal plexus and orthoslices from indicated position (yellow line) used to measure the diameter of the dorsal aorta (DA), the arterio-vascular junction (AVJ) and the caudal vein (CV). Quantification all along the caudal plexus (13 ISV: Inter segmental vessels) (see also Movie 4). (C) Experimental workflow and depletion of ITGB1 via siRNA in D2A1 cells: control siRNA (siCTL), and two distinct sequences of the siRNA targeting ITGB1 (siITGB1#1, siITGB1#2). Representative western-blot (WB) and immunofluorescent

images are shown. Quantification of ITGB1 levels using WB is also provided (n=3). (D) Heatmaps of arrested CTCs after 3hpi are shown for CTCs transfected with siRNAs (n=77, 63, 55, respectively). (E) Quantification of the ratio of arrested CTCs in the indicated region is provided. Norm.: normalized to siCTL AVJ. (F) Graph depicts the number of adhesion events (CTCs to HUVECs) quantified in our microfluidic approach (n=3 independent experiment) (See also Movies 6&7). Norm.: normalized to siCTL. (G) Experimental set-up of intravital CLEM performed on arrested CTCs only 15 mpi (minutes post-injection). Representative EM images of arrested CTCs (red) in vascular lumen (green) are provided from two different sections (top and bottom). A reconstruction of an Electron Tomogram is provided. (H) Experimental set-up, representative image and quantification of optical tweezing experiments of arrested CTCs in the AVJ (n=37 arrested cells, n>10 embryos) (see also Movie 8). Values in (A), (C), (E) and (F) are mean ±SD. *p <0,05, **p < 0.01, ***p <0.001. Mann-Whitney test for (E), Krustal-Wallis test and Dunn's multiple comparisons post-test for (F).

Figure 3: Modulating blood flow forces regulates arrest of CTCs. ZF embryos were treated with vehicles, lidocain (A-F) or IBMX (G-L). (A,G) Experimental workflow. Heart pacemaker activity is quantified for each condition. CTL: Breeding water. An additional kymograph analysis is provided. (B,H) (top) Images extracted from fast imaging and PIV analysis of the blood flow in the caudal plexus (region boxed in A,G) (see also Movies 9&10). (Bottom) Quantification of the flow profile in the center of the dorsal aorta analyzed at position ISV 8, ISV 4 and ISV1 (n=4 to 5 embryos per condition). (C,I) Orthogonal flow velocity profile and quantification extracted from optical tweezing of RBCs in the dorsal aorta under ISV 1 (W,Wall; C,Center) (See also Movie 11). (D,J) Experimental workflow and representative images of the residency time of CTCs in the caudal plexus over a period of 5 min (See also Movies 13). Arrow heads indicate long lasting arrested cells (white color). (E,K) Spatio-temporal quantification of the residency time of CTCs in the CP using heatmapping on a representative embryo. (F,L) Quantification of the ratio of CTCs as well as the mean arrest time over a period of 5 min for embryos treated with vehicle or the indicated drug. Norm.: normalized to vehicle mean. Values in (A-C), (F), (G-I) and (L) are mean ±SD. *p <0,05, **p < 0.01, ***p <0.001, ****p <0.0001. Mann-

Whitney test for (C,F,I,L), Kruskal-Wallis and Dunn's multiple comparisons post-test for (A,G).

Figure 4: Modulating blood flow forces regulates stable intravascular adhesion of CTCs. ZF embryos were treated with vehicles, lidocain (A-C) or IBMX (D-F). (A,D) Experimental workflow and representative images of arrested CTCs (red) in the caudal plexus (green) of vehicle- or drug-treated embryos. (B,E) Quantification of the number and location of arrested CTCs in the caudal plexus of 3hpi vehicle- or drug-treated embryos, through heatmapping. (C,F) Quantification of the number of arrested CTCs per embryo as well as the ratio of arrested CTCs per region in vehicle- or drug-treated embryos, 3 hpi. Data normalized to vehicle AVJ mean ratio. Values in (C) and (F) are mean ±SD. *p <0,05, **p < 0.01, ****p <0.0001. Mann-Whitney test.

Figure 5: Blood forces control the extravasation of CTCs. ZF embryos were treated with vehicle, lidocain (A-B) or IBMX (C-D). (A,C) Representative images of TCs (red) in the caudal plexus (green) of 24 hpi vehicle- or drug-treated embryos are shown. 3D reconstruction and scheme of the boxed region is also provided. (B,D) Quantification of the number and location of intra- and extravascular TCs in the caudal plexus of 24hpi vehicle- or drug-treated embryos, through heatmapping. Quantification of the ratio of extravascular TCs is also provided. Data normalized to vehicle mean ratio. (E) Experimental workflow and CLEM analysis of 24 hpi vehicle- or lidocain-treated embryos is used for further assessing the vascular location of TCs (yellow stars) intravascular (red) or extravascular (blue) (See also Movie 14). CLEM: Correlative light and electron microscopy. Values in (B) and (D) are mean ±SD. *p <0,05, ****p <0.0001. Mann-Whitney test.

Figure 6: Extravasation of CTCs occurs via flow-dependent endothelial remodeling. (A) Experimental workflow. (B) Extracted Z-projection image from 3D time-lapse analysis of the behavior of arrested TCs (red) in the caudal plexus vasculature (green) over a period of 15h (See also Movie 15). (C) Multiple sequential images, over a period of 800 min, of the region boxed in B are displayed and commented (yellow arrowheads point to the location of the associated comment (left panel)). (D) Multiple sequential images, over a period of 150 min, of the region boxed

in B are displayed and commented (yellow arrowheads point to the location of the associated comment). (E) Experimental workflow and CLEM analysis of a 9hpi vehicle-treated embryo. Extracted images of confocal analysis of extravasating TCs (red) at 9hpi is performed. (F) TEM image of the region of interest boxed in E, retrieved in the electron microscopy volume. A representative section is shown and color-coded for TCs (red) and vascular lumen (green) (see also Movie 16). (G) 3D reconstruction of the serial section TEM performed over the entire ROI, depicting TCs (red) and associated ECs (green) (See also Movie 16). (H) Electron tomography image extracted from 3D reconstruction over the boxed region in F (TC: red, ECs: green) (see also Movie 16). (I) Representative images of TCs (red) and the associated vasculature (green) in 9 hpi embryos are shown. (J-K) Quantification and kinetic analysis of the mean number of events over time for vehicle and lidocain treated embryos. The number of events (intravascular, pocketing and extravascular) was quantified at 3hpi (vehicle: n=16, 72 events and Lidocain: n=21, 78 events), 9 hpi (vehicle: n=22, 95 events and Lidocain: n=23, 110 events) and 24 hpi (vehicle: n=20, 94 events and Lidocain: n=20, 104 events). Immunostaining (L) of TCs (LifeAct, red) arrested on a monolayer of HUVECs (PECAM, green) is shown, in two flow conditions (0 and 400/sec). Height of associated HUVECs is color-coded and displayed. (M) Quantification of the number of transmigrated TCs and of transmigrated TCs with remodeled HUVECs. Values in (M) are mean ±SD. *p <0,05, ***p <0.001, ****p <0.0001. Fisher test for (M).

Figure 7: Permissive flow profiles favor formation of micrometastasis in the mouse brain. (A) Experimental workflow and representative images of micrometastases in 7 dpi mice injected with Jimt1-GFP cells (2PM: Two-photon microscopy). (B) Experimental workflow and 3D reconstruction of representative vascular network of the healthy brain. Quantification of the mean blood flow velocity in brain capillary with a diameter of 5 to 10 µm (highlighted in green, where extravasation preferentially takes place) and with higher diameter (highlighted in red, where extravasation is not expected). Work done over more than 5,000 tumor cells from four different tumor cell lines were quantified (JIMT1br3, A2058br, PC14PE6br, H1). A total of 51-96 vessels from 12-13 regions (dimensions: 607.28x607.28x372.00 µm) of 3-6 animals per group were quantified. Box plots representing median values with 10th, 25th, 75th and 90th percentiles. ***p <0.001 (Mann-Whitney test). (C)

Experimental workflow of intravital CLEM of 3dpi arrested JIMT1br3 cells. Maximum Z-projections showing an arrested JIMT1br3 cell (GFP, green) and the associated vasculature (TRITC-dextran, red). Merged images of the micro-computed x-ray tomography (mCT) and the intravital imaging (IVM) volume. Vessels containing the TC is circled in green (TC) and dissected using serial section TEM in D, normal neighboring vessels are circled in blue (#1-3) and dissected in E. (D) Serial section TEM images and segmentation of the tumor cell (green), its nucleus (blue) and ECs (red colors) are shown. 3 different z heights are provided. (E) TEM images and segmentation of the ECs (red colors) of normal neighboring vessels are shown.

Figure 8: Blood perfusion controls the location of human brain metastases (BM). (A) Number of BM and number of patients are provided for the entire cohort. BM originate from various tumor types including lung cancer (n=51), skin cancer (n=17), breast cancer (n=10), genitourinary (GU) cancer (n=10), gastrointestinal (GI) cancer (n=4), sarcoma (n=2) and cancer of unknown primary origin (n=6). (B,C) BM of the 100 patients were segmented semi-manually and co-registered on a CT perfusion mask from a control brain template consisting of 107 healthy patients. The cerebral blood flow (CBF) mask is displayed with red indicating a lower CBF and yellow a higher CBF. The cumulative BM is overlaid to the perfusion mask. (D) Mean CBF (cerebral blood flow) and MTT (mean transit time) is displayed for the brain metastases (BM, +) and the corresponding area without any BM (BM, -). Bars indicate standard deviations. Paired sample t-test (voxel-wise analysis) was used to compare the perfusions values of the BM+ and BM- regions. (E) Graphical abstract of our study: we identified a threshold of flow velocities that are permissive for the arrest of CTCs, a prerequisite for metastasis formation. Below blood flow velocities of 400-600 µm/s, arrest and adhesion of CTCs to the endothelium is favored. This is the case *in vitro* (microfluidics), in zebrafish embryos and in mouse brain capillaries. Similar results are obtained in humans where a significant reduction of blood perfusion is observed in pro-metastatic regions. In a second step, blood flow is required to stimulate endothelial remodeling and subsequent pro-metastatic extravasation. However, although low flow allows arrest of CTCs, it impairs extravasation of arrested TCs. Thus, pro-metastatic vascular regions are characterized by flow profiles that are sufficiently low (or reduced) to favor the arrest of CTCs, and sufficiently high to stimulate endothelial remodeling.

SUPPLEMENTARY MATERIALS

Supplementary figure legends

Figure S1. Related to Figure 1: CTCs arrest and extravasate in the brain of ZF embryos. (A) Experimental workflow. (B) Maximum projection of confocal stack of the ZF brain vasculature (green) containing extravasated TCs (red). White square indicates the position of high magnification images shown on the right. (C) Blood flow velocity measurement in the vessel close to two extravasated TCs (from B). Individual tracks of single RBCs are shown.

Figure S2. Related to Figure 1: Flow drop in the CP occurs upon *in silico* 3D flow simulation (A) Confocal Z-projection of ZF posterior caudal plexus (CP) at 2 dpf. (B) Partial 3D segmentation (Amira) based on confocal acquisition (A). (C) Simplified AOC model of the ZF CP. (D) Image extracted from Movie S3, showing flow simulation results in the AOC model. (E) Velocity profiles obtained from flow simulation at several positions indicated in C. (F) Graphical representation of minimum, maximum and mean values of the blood flow velocity over the 5 positions from C.

Figure S3. Related to Figure 2: Identification of early adhesion forces using OT *in vitro*. (A) Experimental set up and quantification of the measured adhesion rupture force (n=8) of attached TC (top). Annotated image sequence from Movie 6 showing the detachment of a TC from the endothelial monolayer (bottom). (B) Experimental set up and quantification of the ratio of effective adhesion events upon OT (left) and OT-mediated detachment events (right) using siRNA-treated TCs. Values are mean ±SD. *p <0,05, **p <0.01. Ficher test.

Figure S4. Related to Figure 3: Tuning PMA for tuning hemodynamic profiles *in vivo*: side-analysis and OT measurement. (A) Experimental workflow, and a representative image of the PIV analysis in the CP. Quantification of the duration of the flow under 400 µm/sec for each pharmacological condition in the dorsal aorta (position ISV 1, 4 and 8 from A) (n = 4 to 5 embryos per condition). (B) Experimental workflow of OT-mediated quantification of hemodynamic forces *in vivo* and annotated image showing trapped RBC in the DA (yellow) (see also Movie 11). Quantification

and mapping of the flow force measured with OT on trapped RBCs for 3 conditions: lidocain, IBMX and control (breeding water). Values in A are mean ±SD.

Figure S5. Related to Figure 3: Tuning of flow profiles using PMA modulators is confirmed using *in silico* 3D flow simulations. (A) AOC model of the ZF posterior plexus. (B and D) Image extracted from Movie 10, showing flow simulation results in the AOC model for vehicles and lidocain (B) or IBMX (D). (C and E) Velocity profiles from flow simulation at several positions for each condition (as shown in A). CV: caudal vein.

Figure S6. Related to Figure 3: Blood flow tuning does not affect the architecture of the caudal plexus or tumor cells ability to migrate and adhere. (A) 3D segmentation (IMOD) from one ZF posterior caudal plexus per condition (See also Movie 12). (B) Quantification of the total vascular surface from dorsal aorta (DA, red on A) and caudal veins (CV, blue on A) for each condition (n=3). (C) Quantification of the number of vascular loops for each condition (n=3). (D) Representative images of embryos injected with dextran 500kDa and imaged 3 hpi are shown (E) Representative images of wound closure for each condition 0, 9 and 24 hours after wound. (F) Quantification of the wound closure over time (n=3). (G) Representative image of TC stained with crystal violet during the adhesion test (left). Quantification of the absorbance measured at 590nm in the 4 conditions (right). Experiment was done 3 times, in triplicate. Values in (B-C) and (E-F) are mean ±SD. *p <0,05, **p <0.01. Mann-Whitney test.

Figure S7. Related to Figure 8: Tuning PMA with two other drugs also perturb the behavior of CTCs in vivo. (A) Quantification of the PMA with nifedipin (5µM) treatment compared to vehicle. (B) Number and location of arrested CTCs 3hpi using heatmapping, and quantification (C). (D-E) Adhesion and migration assay results of TCs assessed in presence of nifedipin. (F) Quantification of the PMA with norepinephrine (500µM) treatment compared to control. (G) Number and location of arrested CTCs 3hpi using heatmapping, and quantification (H). Data normalized to vehicle AVJ mean. (I-J) Adhesion and migration of TCs is assessed in presence of

norepinephrine. Values in (A), (C-F) and (H-J) are mean ±SD. *p <0,05, **p <0.01. Mann-Whitney test for (A,D,F,H).

Supplementary movie legends

Movie S1. Related to Figure 1: CTCs arrest and extravasate in the brain of ZF embryos. Low (top-left) and high-magnification (right) confocal Z-stack of the ZF head vasculature (green), containing two extravasated TCs (red). (bottom-left) high-speed imaging of the blood flow in the vessel of extravasated TCs.
https://www.dropbox.com/s/j7v24yip3ajgnk9/Movie_1_Follain_et_al.mp4?dl=0

Movie S2. Related to Figure 1: Blood flow drops along the arterial vasculature of the ZF embryo. Whole-embryo high-speed flow acquisition and PIV analysis. A selection of 4 regions of interest reveal the significant flow drop in the caudal region. Color code = velocity ranging from 2500 (red) to 50 µm/sec.
https://www.dropbox.com/s/195pn49ztf4gjt0/Movie_2_Follain_et_al.mp4?dl=0

Movie S3. Related to Figure S2, related to Figure 1: Flow drop in the caudal plexus occurs *in silico*. 3D reconstruction of the caudal plexus is used for blood flow simulation.
https://www.dropbox.com/s/11j1ycuqv19t3hg/Movie_3_Follain_et_al.mp4?dl=0

Movie S4. Related to Figure 2: Fine vascular architecture of a 2-dpf ZF embryo. 3D reconstruction of the vascular architecture of a 2-dpf ZF embryo, upon two-photon excitation microscopy.
https://www.dropbox.com/s/dyy6mu0y7ku8ae3/Movie_4_Follain_et_al.mp4?dl=0

Movie S5. Related to Figure 2: Stable adhesion and intravascular migration of CTCs. Time-lapse analysis of the intravascular adhesion of TCs (red) to the endothelium (green) of 2-dpf embryos (*Tg(fli1a:egfp)*), in the caudal plexus. Two different z position are provided.
https://www.dropbox.com/s/1j8flu4ke32u913/Movie_5_Follain_et_al.mp4?dl=0

Movie S6. Related to Figure S3, related to Figure 2: Identification of early adhesion forces of CTCs to ECs. Transmitted light imaging of OT experiments *in vitro* shows the adhesion and its rupture between a single CTC (trapped) and ECs. The plot displays the extracted adhesion resistance force for this event. Adhesion to

EC imposes a growing force (25-40 sec) before its break, visible on the graph with the drop of force measured (40-45 sec).
https://www.dropbox.com/s/2vmu84x548zwe2k/Movie_6_Follain_et_al.mp4?dl=0

Movie S7. Related to Figure S3, related to Figure 2: Depletion of ITGB1 impedes the early adhesion of CTCs to ECs. Transmitted light imaging of optical trapping of siCTL versus siITGB1 cells. Stable adhesion of the CTC to the EC monolayer is visible in the control situation (See time=20s). No adhesion is visible for siITGB1 cells.
https://www.dropbox.com/s/ahipj1ume0wtrzn/Movie_7_Follain_et_al.mp4?dl=0

Movie S8. Related to Figure 2: Early adhesion forces of CTCs to ECs *in vivo* rapidly exceed 200 pN. X,Y and Z movement of the optical trap *in vivo* has no effect on arrested CTCs in the dorsal aorta. Successful trapping of RBCs in close contact with the arrested CTC, which remains attached to ECs, shows that adhesion forces rapidly exceed 200 pN *in vivo*.
https://www.dropbox.com/s/r6o17w3irglpp2s/Movie_8_Follain_et_al.mp4?dl=0

Movie S9. Related to Figure 3: Tuning the blood flow in the CP of 2-dpf ZF embryos. High-speed flow acquisition (200 fps) and PIV analysis in the CP of vehicle- or drug-treated ZF embryos. Color code = velocity ranging from 1600 (red) to 400 µm/sec.
https://www.dropbox.com/s/gxp6xu8mbwn4duk/Movie_9_Follain_et_al.mp4?dl=0

Movie S10. Related to Figure S4, related to Figure 3: In silico tuning of the blood flow in the virtual CP. 3D reconstruction of the CP is used for blood flow simulation. Flow frequencies measured *in vivo* are used (values in brackets).
https://www.dropbox.com/s/ay9iv3hnfqiinxv/Movie_10_Follain_et_al.mp4?dl=0

Movie S11. Related to Figure S4, related to Figure 3: Tuning and measuring hemodynamic forces *in vivo*. Transmitted light imaging of OT of RBCs performed in the DA of ZF embryos. Movie(s) show efficient trapping of RBCs in the DA and the CV. Red circle = OT.
https://www.dropbox.com/s/pmw8rmgsbtvj28u/Movie_11_new_Follain_et_al.mp4?dl=0

Movie S12. Related to Figure S6, related to Figure 3: Tuning the blood flow does not perturb the vascular architecture of the CP. 3D segmentations of the caudal plexus in the 4 different conditions are shown. Dorsal aorta appears in red, caudal veins in blue.
https://www.dropbox.com/s/6sefnvfz9tu0u89/Movie_12_Follain_et_al.mp4?dl=0

Movie S13. Related to Figure 3: Tuning blood flow forces perturbs the early arrest of CTCs in living ZF embryos. Instantaneous live imaging of CTCs (red) upon intravascular (green) injection in vehicle- or drug-treated ZF embryos reveals that blood flow affects the early arrest of CTCs. Final Color code is based on time of arrival and residency of tumor cells (Image J).
https://www.dropbox.com/s/9yu27sj3u3bgsm4/Movie_13_Bis_Follain_et_al.mp4?dl=0

Movie S14. Related to Figure 5: CLEM of extravasated TCs in the ZF embryo. Confocal imaging and correlative serial TEM of TCs reveal the extra- and intra-vascular location.
https://www.dropbox.com/s/1whmyfkt7zd4pfk/Movie_14_Follain_et_al.mp4?dl=0

Movie S15. Related to Figure 5: Extravasation of arrested CTCs in the caudal plexus of a ZF embryo. 3D time-lapse confocal imaging of arrested CTCs (red) in the CP (green) over 15h. Extravasation of CTCs occurs mostly upon ECs pocketing and remodeling.
https://www.dropbox.com/s/222fw083nkbkf6n/Movie_15_Follain_et_al.mp4?dl=0

Movie S16. Related to Figure 6: Vascular pocketing and remodeling drives extravasation of arrested CTCs. Confocal imaging, correlative serial TEM and electron tomography of extravasating TCs (red) shows discrete pocketing by ECs (green).
https://www.dropbox.com/s/lgbgad510hdf2ps/Movie_16_Follain_et_al.mp4?dl=0

METHODS

Cell culture and siRNA-mediated knock-down

D2A1 stably expressing LifeAct-RFP or LifeAct-YPET, kindly provided by Robert A. Weinberg (MIT), were grown as previously described[64], in DMEM with 4.5 g/l glucose (Dutscher) supplemented with 5% FBS, 5% NBCS, 1% NEAA and 1% penicillin-streptomycin (Gibco). Human Umbilical Vein Endothelial Cells (HUVEC) (PromoCell) were grown in ECGM (PromoCell) supplemented with supplemental mix (PromoCell C-39215) and 1% penicillin-streptomycin (Gibco). To maximize the reproducibility of our experiments, we always used these cells at 4th passage in the microfluidic channels. siRNAs were transfected into D2A1 cells using Lipofectamine RNAiMAX (Invitrogen) following the manufacturer's instructions. Experiments were performed between 72 h and 96h post-transfection. siRNA sense sequences are the following: siCTL: GCA AAT TAT CCG TAA ATC A, siITGB1 #1: CCA CAG AAG UUU ACA UUA A, siITGB1 #2: GUG UGU AGG AAG AGA GAU A.

Zebrafish handling

Tg(fli1a:eGFP) Zebrafish (*Danio rerio*) embryos from a Tübingen background used in the experiments were kindly provided by the group of F.Peri from EMBL (Heidelberg, Germany). Embryos were maintained in Danieau 0.3X medium (17,4 mM NaCl, 0,2 mM KCl, 0,1 mM $MgSO_4$, 0,2 mM $Ca(NO_3)_2$) buffered with HEPES 0,15 mM (pH = 7.6), supplemented with 200 µM of 1-Phenyl-2-thiourea (Sigma-Aldrich) to inhibit the melanogenesis, as previously described[38].

Pharmacological treatments

Drugs were added in the breeding water (Danieau 0.3X + PTU) of the embryos before mounting and injection. IBMX (3-isobutyl-1-methylxanthin)[40], lidocain[39], nifedipin and norepinephrine[40] (Sigma) were used at 100 µM in DMSO (incubation time: 20h), 640µM in ethanol (inc. time: 2h), 5 µM in DMSO (inc. time: 2h) and 500 µM in water (inc. time: 1h) respectively.

High-speed microscopy for pacemaker activity and blood flow profiling

To measure the heart pacemaker activity and the associated blood flow profiles, we used the USB 3.0 uEye IDS CCD camera (IDEX) mounted on a DMIRE2 inverted

microscope (Leica) using transmitted light. Heartbeats were acquired at 80 frames per second (fps) and blood flow in the tail region at 200 fps. For the whole-embryo high-speed recordings of the blood flow, acquisitions were done using an Orca Flash 4.0 cMOS camera (Hamamatsu) mounted on an IX-73 inverted microscope equipped with a UPLFLN 10X/0.3 objective (Olympus). Heartbeats were manually counted to compute the pacemaker activity. The blood flow intensity profile over time at each positions in the vasculature was analyzed using an adapted Particle Image Velocimetry (PIV) protocol from ImageJ software that is available online (https://sites.google.com/site/qingzongtseng/piv).

Intravascular injection of CTCs in the ZF embryo

48 hour post-fertilization (hpf) *Tg(Fli1a:eGFP)* embryos were mounted in 0.8% low melting point agarose pad containing 650 µM of tricain (ethyl-3-aminobenzoate-methanesulfonate) to immobilize the embryos. D2A1 LifeAct-RFP cells were injected with a Nanoject microinjector 2 (Drummond) and microforged glass capillaries (25 to 30 µm inner diameter) filled with mineral oil (Sigma). 23nL of a cell suspension at 100.10^6 cells per ml were injected in the duct of Cuvier of the embryos under the M205 FA stereomicroscope (Leica), as previously described[30].

Confocal imaging and analysis

Confocal imaging was alternatively performed with an upright TCS SP5 or SP8 confocal microscope with a HC FLUOTAR L 25X/0,95 W VISIR (Leica), or with a SP2 confocal head mounted on a DMIRE2 stage with HC PL APO 20X/0,7 IMM CORR CS objective (Leica). The caudal plexus region (around 50µm width) was imaged with a z-step of less than 1.5 µm for at least 20 embryos per conditions from at least 3 independent experiments. Cells dispersion was manually counted and localized (using the stereotype patterning of ISVs as reference) in the caudal plexus. The data were compiled to generate heatmaps using a custom-made MATLAB plug in (see next section). Post-processing was performed using Imaris (Bitplane), Amira (FEI) and IMOD (Boulder Laboratory, University of Colorado) for segmentation and 3D reconstruction. For the permeability assay, embryos were pharmacologically treated (as described above) and injected in the duct of Cuvier with 18,4 nl of Dextran-TRITC (500kDa), 3 hours before confocal imaging of the caudal plexus. For assessing the endothelial remodeling *in vivo*, cells were sorted in 3 groups

(intravascular, pocketing and extravascular) based on confocal imaging. A kinetic analysis for the individual groups, in vehicle- and lidocain-treated embryos, was performed based on a Michaelis-Menten model, where the arrested tumor cells (TC) interact with endothelial cells (EC) that initiate pocketing (P) before undergoing extravasation (Ex):

$$[EC] + [TC] \rightleftharpoons [P] \rightarrow [Ex]$$

Heatmaps

The heatmaps were generated using ImageJ (https://imagej.nih.gov/ij/index.html) and MATLAB (MathWorks) softwares. The adhesion/extravasation events are identified for each fish after the analysis of the confocal z-stacks with ImageJ. The position of these events is manually reported on a gray-level support image of a 2.5 days post-fertilization zebrafish plexus. Then, all the support images representing each embryo for one condition were put together in an image stack using ImageJ. The stack is read layer by layer in MATLAB and the dots representing the localization are automatically detected with the function Hough circles (Yuan-Liang Tang, Department of Information Management, Chaoyang University of Technology, Taichung, Taiwan) (https://fr.mathworks.com/matlabcentral/fileexchange/22543-detects-multiple-disks--coins--in-an-image-using-hough-transform) using the Circular Hough Transform based algorithm, giving in output the coordinates of the detected dots. Gaussian spots are then created at these coordinates. The amplitude of each Gaussian spot is equal to 1. The different layers of one condition are added each other by making a sum projection, and a black and white mask created with the gray level support image is applied to this sum projection. The gaussian spot amplitudes of each layers are summed to produce the heatmap. The areas of the sum projection where the gaussian spot amplitudes are higher corresponds to high density areas of adhesion/extravasation events. To produce the final heatmap, a custom colormap, inspired by the jet colormap, is applied to the sum projection. The colormap goes from black (no event) to red (high density areas).

Sample preparation for Electronic microscopy of ZF embryos

Correlative Light and Electron Microscopy was performed as previously described[38]. To describe ultra structural characteristics of CTCs and the endothelium in the ZF embryo, chosen ZF embryos were chemically fixed with 2,5% glutaraldehyde and 4%

paraformaldehyde in 0.1 M Cacodylate buffer (fish tails cut off in the fixative). Samples were kept in fixative at room temperature for 1-2h and stored in fixative at 4°C overnight or until further processing. Samples were rinsed in 0.1M Cacodylate buffer for 2x5min and post-fixed using 1% OsO4 in 0.1 M Cacodylate buffer, for 1h at 4°C. Then, samples were rinsed for 2x10min in 0.1M Cacodylate buffer and secondary post-fixed with 4% water solution of uranyl acetate, 1h at room temperature. Rotation was used at all steps of sample processing. Followed by 5min wash in MiliQ water, the samples were stepwise dehydrated in Ethanol (25%, 50% each 15min, 95%, 3X100% each 20min) and infiltrated in a graded series of Epon (Ethanol/Epon 3/1, 1/1, 1/3, each 45min). Samples were left in absolute Epon (EmBed812) overnight. The following day, samples were placed in a fresh absolute Epon for 1h and polymerized (flat embedded) at 60°C for 24-48h. Once polymerized, most surrounding Epon was cut off using razorblade and samples were mounted on empty Epon blocks (samples flat on the top of the blocks) and left at 60 °C for 24h-48h. Semi-thin sections (200nm) were serially sectioned using ultramicrotome (Leica Ultracut UCT), collected on formvar-coated slot grids and stained with 4% water solution of uranyl acetate for 10min and Reynolds lead citrate for 3min. Semi-thin sections (200nm) were imaged with a CM120 transmission electron microscope (Philips Biotwin) operating at 120 kV. Images were recorded with Veleta 2k x 2k (Olympus-SIS) camera using iTEM software. On the same sections, Electron tomography was performed with a Tecnai F30 Field Emission Gun TEM (FEI) operating at 300 kV and equipped with an Eagle 4K camera (FEI). The F30 was controlled by Tecnai User Interface (PEOUI) and Tecnai Acquisition (TIA) software. Single-axis tomograms were obtained using SerialEM and reconstructed in eTomo, part of the IMOD software package (Boulder Laboratory, University of Colorado).

Microfluidic experiments

Quantification of the flow-dependent adhesion of CTCs was done using six channels µ-slides $VI^{0,4}$ pre-coated with fibronectin (IBIDI). HUVEC cells were seeded at 21 000 cells per channel (Volume = 30µl). Medium was changed twice a day until they reach maximal confluency (3 to 4 days). D2A1 LifeAct-GFP cells were diluted to maintain the concentration of 150 000 cells/ml of cells between the different speed conditions and perfused using a REGLO Digital MS-2/12 peristaltic pump (Ismatec) and Tygon

LMT-55 tubing (IDEX) for 10 minutes before fixation with 4% PFA (Electronic Microscopy Sciences) and stainings (see below).

For endothelial remodeling experiments *in vitro*, two µ-slides $I^{0.4}$ Luer (IBIDI) coated with fibronectin from bovine plasma at 10µg/ml (Sigma F-1141) were used in parallel for each experiment. After seeding the HUVEC cells, one channel was cultured under a flow of 400µm/sec using REGLO pump and Tygon tubbing and for the other channel (no flow condition), medium was changed twice a day. At confluence, D2A1 LifeAct-RFP cells were added at a concentration of 200 000 cells/ml for 10 min. Then, tumor cells were washed using fresh medium and incubated for 16h with or without flow. Z position of the tumor cells relative to the HUVEC monolayer was determined using the piezzo stage of the confocal microscope.

Optical tweezers

Optical tweezing experiments were performed as previously described[31]. Briefly, OT behaves as a picodynanometer where stiffness and the displacement from the steady position can be computed to extract the applied force. Optical tweezing experiments *in vitro* were performed in single channel $I^{0.4}$ Luer µ-slides pre-coated with fibronectin (IBIDI). HUVEC cells were cultured until confluence before the experiment as described above. D2A1 were perfused at 10^4 cells/ml at a low speed to maximize the cell trapping and avoid collision effects by other CTC. A 1064 nm laser (Navigator 1064-7Y Spectra Physics) was used to generate optical tweezers mounted on a thermostated inverted microscope equipped with a UPLFLN-P 100X/1.3 objective (Olympus). D2A1 cells attached to the HUVEC monolayer were trapped in the beam and moved away from the HUVEC monolayer by displacing a computer-controlled piezzo stage (PI P545 PNano) along the X/Y axis. The fluctuations of the cell in the trap were recorded on a quadrant diode (Thorlabs PDQ30C) and the associated spectral power density allowed the calibration of the trap stiffness. The detachment of D2A1 cells from the HUVEC monolayer was recorded using a Cmos camera (Thorlabs DCC3240C). The movies were analyzed to access the center of mass of the cell in each image. This position compared to the steady position of the cell in the trap is proportional to the force exerted on the cellular adhesion. The rupture force between D2A1 and HUVEC gave rise to a drop in the position of the trapped cell steady state and allowed to access the rupture force.

Optical tweezing experiments in the zebrafish embryo were performed as previously described[31], with slight modifications: We implemented the setup with a thermoregulated chamber ensuring the embryos to remain at 28°C. We acquired the displacement with the camera at high frame rates 200fps after having established the power spectrum from the photodiode at 20kHz resolution to calibrate the setup.

Mice experiments and surgical procedures

8-10 weeks old female Nu/Nu mice (Charles River, Sulzfeld, Germany) were used to study the extravasation cascade. All efforts were made to minimize animal suffering and to reduce the number of animals used. The operation of the chronic cranial window was done as previously described[7,65]. Three weeks after window implantation a 100µl cell suspension, containing 500,000 tumor cells (JIMT1br3, A2058br, PC14PE6br, H1), was injected intracardially. *In vivo* imaging was done on day 3 and day 7 after the heart injection. After imaging, the mouse was perfusion-fixed through intracardiac injection with 2.5% glutaraldehyde (Electron Microscopy Sciences, Hatfield, PA) and 2% formaldehyde (Electron Microscopy Sciences) in 0.1 M PHEM buffer (comprising 60 mM PIPES, 25 mM HEPES, 10 mM EGTA and 2 mM MgCl, pH adjusted to 6.9). Following fixation, the regions of interest (ROIs) were imaged again based on the stored stage *x*,*y*-coordinates. NIRB was performed with the same laser that had been used for *in vivo* microscopy, tuned to 800 nm wavelength, as previously described[29]. Above the ROIs, at the level of the brain surface, a 150×150 μm^2 area was scanned in a single focal plane until the NIRB square became clearly visible through emission of autofluorescence in the green channel. Around the ROI, three bigger 300×300 μm^2 NIRB squares were drawn in non-symmetric positions to facilitate orientation and retrieval of the ROI upon dissection. The brain was removed from the skull and post-fixed by immersion in the same fixative at 4°C overnight. The following day, the fixative was replaced with 0.1 M PHEM buffer, and the brain was stored at 4°C until further processing[29]. All animal procedures were performed in accordance with the institutional laboratory animal research guidelines after approval of the Regierungspräsidium Karlsruhe, Germany (governmental authority).

***In vivo* multiphoton laser scanning microscopy (MPLSM).**

In vivo imaging was performed with a Zeiss 7MP microscope (Carl Zeiss Microscopy, Jena, Germany) provided with a Coherent Chameleon UltraII laser (Coherent,

Glasgow, UK) with a 500-550 nm and a 575-610 nm band pass filter. With the wavelength of 850 nm GFP and TRITC-dextran were detected. To prevent phototoxic effects, laser power was always kept as low as possible. During the imaging process animals were anaesthetized with a low gas narcosis including 1.5% isoflurane (Baxter, Unterschleißheim, Germany) and 98.5% oxygen (Guttroff, Heidelberg, Germany). During imaging body temperature was kept constantly at 37°C by a heating pad. To acquire angiographies of brain blood vessel, 0.1 ml TRITC-dextran (500 kDa, 10 $mg.ml^{-1}$, Sigma-Aldrich, Munich, Germany) was injected.

Blood flow velocity measurements and visualization of MPLSM data.

The blood flow velocity was measured by a line scan with a minimum length of 10 µm, detecting 2000 events in microvessels. At least 16 randomly chosen vessels were measured per animal. The resulting scan identifies single erythrocytes as angular black lines, where the x-axis is according to the length of the detected distance and the y-axis is the elapsed time of the measurement. The angle is converging more and more to 90° when the cells are static. By knowing the resolution of both parameters and by the measurement of the slope of 30 randomly chosen red blood cells a calculation of the mean velocity is possible, by inversion of the result.

Western blotting

For western blotting analysis, extracts corresponding to similar cell numbers were loaded on 4-20% polyacrylamide gels (Biorad) and run under denaturing conditions. The following primary antibodies were used: ITGB1 (Millipore AB1952; rabbit), GAPDH (V-18; Goat). HRP-conjugated secondary antibodies were used with ECL (GE Healthcare) for reading using using a PXi system (Syngene). Intensities were normalized over cellular GAPDH levels.

Immunofluorescent staining in the microfluidic channels

Cells were fixed using 4% PFA (Electronic Microscopy Sciences), permeabilized with 0.2% Triton-X100 (Sigma) and quenched with 2mg/ml $NaBH_4$ (Sigma) 10 min at room temperature before using the following primary antibodies: rat anti-mouse CD29 (9EG7, BD), mouse anti-human CD31 monoclonal primary antibody (MEM-5, Invitrogen). Following secondary antibodies were used: goat anti-rat or mouse

coupled with Alexa Fluor 488 (Invitrogen). Cells were mounted using Vectashield (Vector Laboratories). For fluorescent labelling of the HUVEC cells (Fig.1), Alexa Fluor 568 Phalloidin (Life-technologies) and DAPI (Sigma) were used.

In vitro migration and adhesion assays

For wound healing assay, cells were cultured until confluence in 6-wells plate. The monolayer was scratched with a 20 µl tips and medium was changed with medium supplemented with the corresponding pharmacological treatments. Pictures were taken at time = 0h, 3h, 6h, 9h and 24h. Wound closure was analyze using ImageJ.

For adhesion assay, cells were plated at 20 000 cells/ml in 96-well plate filled with culture medium supplemented with the corresponding pharmacological treatments. After 30 min incubation, wells were washed with PBS, fixed in 4% PFA and stain with 1% violet crystal (VC, Sigma) for 1h at room temperature. VC was washed with PBS and pure DMSO was added to solubilized VC for 30 min under gentle moving. Optical density at 590nm was measured using TriStar^2 plate reader (Berthold).

Statistical analysis from zebrafish, mouse and microfluidic experiments.

Statistical analysis of the results was performed using the GraphPad Prism program version 5.04. The Shapiro-Wilk normality test was used to confirm the normality of the data. The statistical difference of Gaussian data sets was analyzed using the Student unpaired two-tailed t test, with Welch's correction in case of unequal variances. For data not following a Gaussian distribution, Kruskal-Wallis and Dunn's multiple comparisons post-test or the Mann-Whitney test was used. For qualitative data, the Fisher test was used. Illustrations of these statistical analyses are displayed as the mean +/- standard deviation (SD). p-values smaller than 0.05 were considered as significant. *, $p<0.05$, **, $p < 0.01$, ***, $p < 0.001$, ****, $p < 0.0001$.

Mathematical modeling and numerical methods for *in silico* experiments

The *in silico* experiments are developed in the framework of Finite Element Embedded Library in C++, Feel++[66]. To reproduce the blood flow in the ZF arterial and venous systems, we followed these steps: *(i)* build manually using a computer aided design software and generate a discrete computational domain where the entry point is ISV8 (Figure S2C), *(ii)* set up a fluid-structure interaction model between the blood and the endothelium in Feel++ and *(iii)* extract numerical flow rates and

compare with in-vivo experiments. *(i)* The computational domain could not be obtained directly from the *in vivo* measurements. We built the model using a computer aided design software and reproduced an idealized geometry. The discrete computational domain is built of 884221 tetrahedrons. The computational domain is in millimeters and the units of the physical quantities used hereafter are accordingly adapted. *(ii)* In order to simulate the blood flow in the system, we have to consider the interaction between the blood and the endothelium. The blood flow is modeled using the incompressible Navier-Stokes equations and the endothelium is modeled using the linear elasticity model formulated in displacement/pressure due to the quasi-incompressible nature of the endothelium, both models are supplemented by boundary conditions. Regarding the blood flow: *(i)* a Poiseuille flow in the aorta at ISV8 giving by a fit of the experimental data *(ii)* free outflow boundary conditions at the outlet of the venous system. Regarding the endothelium: *(i)* clamped at the inlet of the aorta (ISV8), ***(ii)*** free-stress at the outlets of the venous system and *(iii)* Robin type condition elsewhere to constrain the endothelium by the surrounding tissues (the elastance coefficient is taken as constant). Finally, the model is completed by coupling conditions at the interface between the fluid and the structure stating the continuity of the velocity and the normal stress. The coupling between both is handled using a so-called Robin-Robin scheme[67]. Finally, we use the following setting for the physical parameters: For the blood: Viscosity, f = 2.2e-6 $kg.mm^{-1}.s^{-1}$; Density, f = 1.0e-6 kg/mm^3. For the endothelium: Density, s = 1.2e-6 kg/mm^3; Young Modulus, E = 3 $kg/(mm*s^2)$; Poisson Coefficient = 0.49 (dimensionless). *(iii)* Regarding the space discretization, we use the finite element method to discretize the model described above. We use continuous piecewise polynomials of order 2 for the velocity and order 1 for the pressure in the fluid and we use continuous piecewise polynomials of order 1 for the displacement and order 1 for the pressure in the solid. Regarding the time discretization, we use for the fluid an BDF2 scheme and for the solid we use the Newmark scheme, both are second order in time. The time step is fixed to 5e-3s and the final time is at 4s. The algebraic representation of the fluid and solid model are solved using iterative methods preconditioned with algebraic-factorization type preconditioners enabling fast solves. The fluid-structure interaction coupling is handled with a Picard method that iterates between the fluid and the solid models until the relative increment between two non-linear iterations reaches 1e-5. We conducted the study for the different

pharmacological treatment (IBMX, EtOH, Lidocain, DMSO). Each condition requires high performance computing to solve the equation set. We used 48 cores to solve each configuration to simulate 4s of blood flow. The later ensures that the flow is correctly established.

Patient blood collection for CTC size analysis

Patient blood samples were acquired in accordance to the World Medical Association Declaration of Helsinki and the guidelines for experimentation with humans by the Chambers of Physicians of the State of Hamburg ("Hamburger Ärztekammer"). All patients gave informed, written consent prior to blood draw. Samples were collected from 5 metastatic breast cancer patients into standard 7.5 ml ethylenediaminetetraacetic acid (EDTA) vacutainers and transferred to TransFix® (Cytomark) tubes within 2 h of sample draw. Blood was also collected from a metastatic non-small lung cancer patient directly into either CellSave® (Menarini-Silicon Biosystems), Cell-free DNA BCT® (Streck) or TransFix® preservatives for further analysis. Circulating tumor cells were isolated from whole blood sample by two size based enrichment systems: Both methods have been validated within a large European consortium of 36 partners from academia and industry, CANCER-ID (www.cancer-id.eu). The Parsortix™ system (ANGLE plc, UK) enriches tumor cells from a wide variety of blood tubes and has been described in detail in previous publications[68,69]. In short, the device passes blood into a disposable cassette. This cassette narrows down to a critical gap of 6.5 µm at which all larger cells are retained while smaller cells pass through into the waste, thus drastically reducing white blood cell and erythrocyte background. Due to their larger size and higher rigidity, tumor cells are retained at the gap and can be extracted by reversing the flow within the chamber. The enriched cell fraction is harvested into a cytospin funnel and spun down (190 x g, 5 min). Upon drying overnight, samples can either be frozen at -80 °C or directly stained by immunocytochemistry (ICC). The second size based enrichment system used to process cancer patient samples, was a novel microfluidic filtration device provided by Siemens Healthcare Diagnostics (Elkhart, IN, USA). The system uses a Hamilton STARlet™ robot (Hamilton Company, Reno Nevada) with a specifically developed software allowing for automated enrichment and staining of CTCs from whole blood[70]. Briefly, the blood is passed through a membrane containing pores of 8 µm, enriching for all larger cells. For this, EDTA blood samples

were transferred into TransFix® preservation tubes and incubated overnight. The blood was then transferred to the device together with all reagents necessary for ICC staining of CTCs. Cytospins generated following Parsortix™ enrichment were stained using fluorescently labeled antibodies. ICC included fixation with 4 % PFA, permeabilization with 0.1 % Triton X-100 and blocking using serum albumin. Two pan-Keratin antibodies (clone AE1/AE3, eBioScience and clone C11, Cell Signaling) were combined with a CD45 targeting antibody (REA747, Miltenyi Biotec) and DAPI for cell detection. Cytospins were cover slipped using ProLong® Gold antifade reagent (Invitrogen). For the filtration device, we performed a single ICC staining step using a cocktail of fluorescently labeled antibodies, followed by cover slipping with ProLong® Gold antifade reagent (Invitrogen). Tumor cells were detected by targeting Dy550 labelled keratins (Pan CK – clone AE1/AE3, CK8/18 – clone UCD / PR10.11, CK19 – clone A53-B/A2), multiple Dy650 labelled white blood cell markers (CD45 – clone 9.4, CD66b – clone G10F5) and DAPI, all provided directly by Siemens Healthcare Diagnostics. Cytospins and filtration membranes were evaluated and enumerated manually by fluorescence microscopy. CTCs were classified as pan-keratin positive, CD45 negative and DAPI positive cells. They were photographed using the AxioVision LE64 microscope software (Zeiss) which allows for measurement of lengths with its respective processing tools.

Brain metastasis and blood flow perfusion study

Human patient data showing the link between brain metastasis (BM) and perfusion pattern were obtained on a single-center cohort. The retrospective study was conducted in compliance with the local ethics committee (Ethik-Kommission der Ärztekammer Hamburg, WF-018/15) with a waiver of informed consent. To collect cases, all MRI studies from 01/2014 to 12/2016 were screened for the presence of untreated malignant intra-axial brain tumors (no previous brain surgery or radiation). In total, 407 patients met the inclusion criteria. From the entire cohort, we randomly selected 100 patients (37 women and 63 men).

MRI was performed using a 1.5 Tesla (Magnetom® Sonata, Siemens Healthcare, Erlangen, Germany; Magnetom® Symphony, Siemens Healthcare, Erlangen, Germany, and Magnetom® Avanto, Siemens Healthcare, Erlangen, Germany) in 94 patients or a 3 Tesla scanner (Magnetom® Skyra, Siemens Healthcare, Erlangen, Germany; Ingenia, Philips Medical Systems, Best, The Netherlands) in 6 patients.

Imaging protocol always included axial T1w spin echo with flow compensation and/or three-dimensional T1w gradient echo sequences following weight-adjusted Gadolinium injection (T1w+). If both sequences were acquired the latter one was used for further analysis. Sequence parameters (repetition time, echo time, inversion time, field of view, matrix, pixel size, slice thickness, interslice gap, and number of slices) varied among the different scanners. All BM were subsequently segmented semi-manually using the Analyze Software System 11.0 (Biomedical Imaging Resource, Mayo Clinic, Rochester, MN, USA)[71]. Axial T1w+ MR images of all patients were then automatically co-registered to the Montréal Neurological Institute (MNI) brain by using the FMRIB Software Library (Analysis Group, Oxford, UK) linear registration tool. Correct registration of all T1w+ images and the segmented BM to the MNI brain was secured by visual inspection. Cluster maps comprising all BM of the respective cohort were calculated (Figure 8). Computed tomography was used to build the brain perfusion atlas. Since cancer patients often show an altered cerebral blood flow due to paraneoplastic changes or chemotherapy administration, we decided to use computed tomography (CT) perfusion data from a healthy cohort as reference[72,73]. In brief, 107 patients were triaged by CT perfusion for symptoms of transient ischemic attack but without evidence of ischemia or any perfusion abnormality, infarction or symptoms on follow up, or vascular abnormality as reported elsewhere[74]. Quantitative perfusion maps were obtained for CBF and MTT[75]. All perfusion raw data were processed in a central core-lab on a workstation dedicated for perfusion analysis (Syngo mmwp VE52A with VPCT-Neuro; Siemens Healthcare, Forchheim, Germany) with motion correction and low band temporal noise removal. Non-parenchymal voxels corresponding to bone, vasculature, calcification and cerebrospinal fluid were automatically excluded by adaptive intensity thresholding. Perfusion parameter maps were calculated based on a deconvolution model by least mean squares fitting. All perfusion maps were then affine registered to 1 mm MNI standard space by a precise registration model between the baseline time average of each CT perfusion dataset and a custom CT template in standard space using the FMRIB Software Library 5.0[76]. Mean voxel-wise perfusion parameter maps normalized to standard space were then registered to each individual patient in our study cohort to obtain voxel specific normal perfusion values. Absolute mean cerebral blood flow (CBF in ml/100g brain tissue/min) and mean transit time (MTT in sec) values of all BM were calculated for each voxel of the perfusion mask and each

voxel with a BM. Statistical analysis was conducted using IBM SPSS Statistics® software (IBM® 2011, version 20, Armonk, New York, USA) and R (The R Foundation, version 3.3.1. Vienna, Austria). The differences in CBF and MTT between all BM and BM- voxels were compared by the independent t-test. Voxels with more than one BM were weighted according to the number of BM occurring within the voxel. The paired samples t-test was used to compare the perfusion values and the volume of the BM. If not otherwise indicated, data are given as median ± interquartile range.

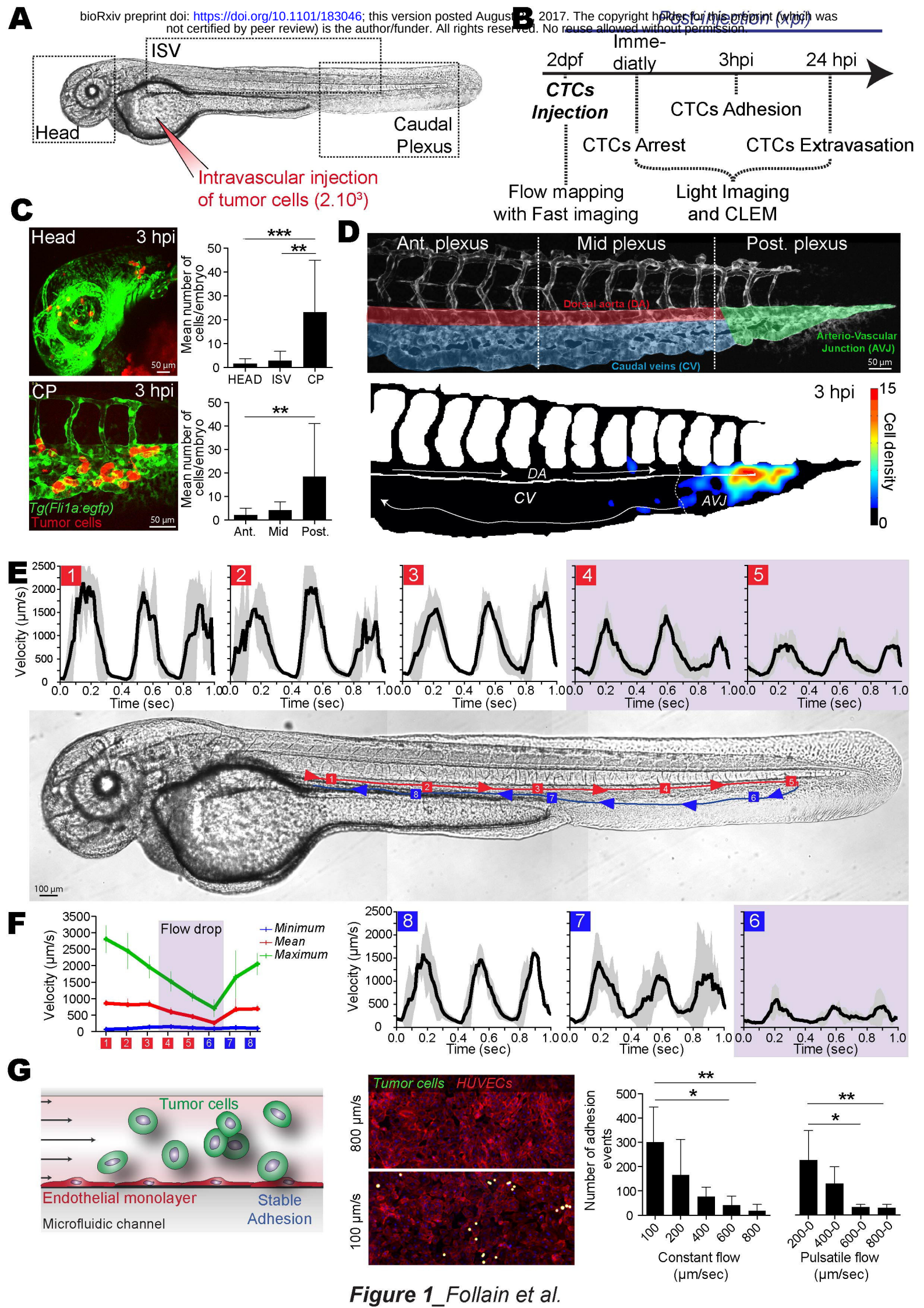

Figure 1_Follain et al.

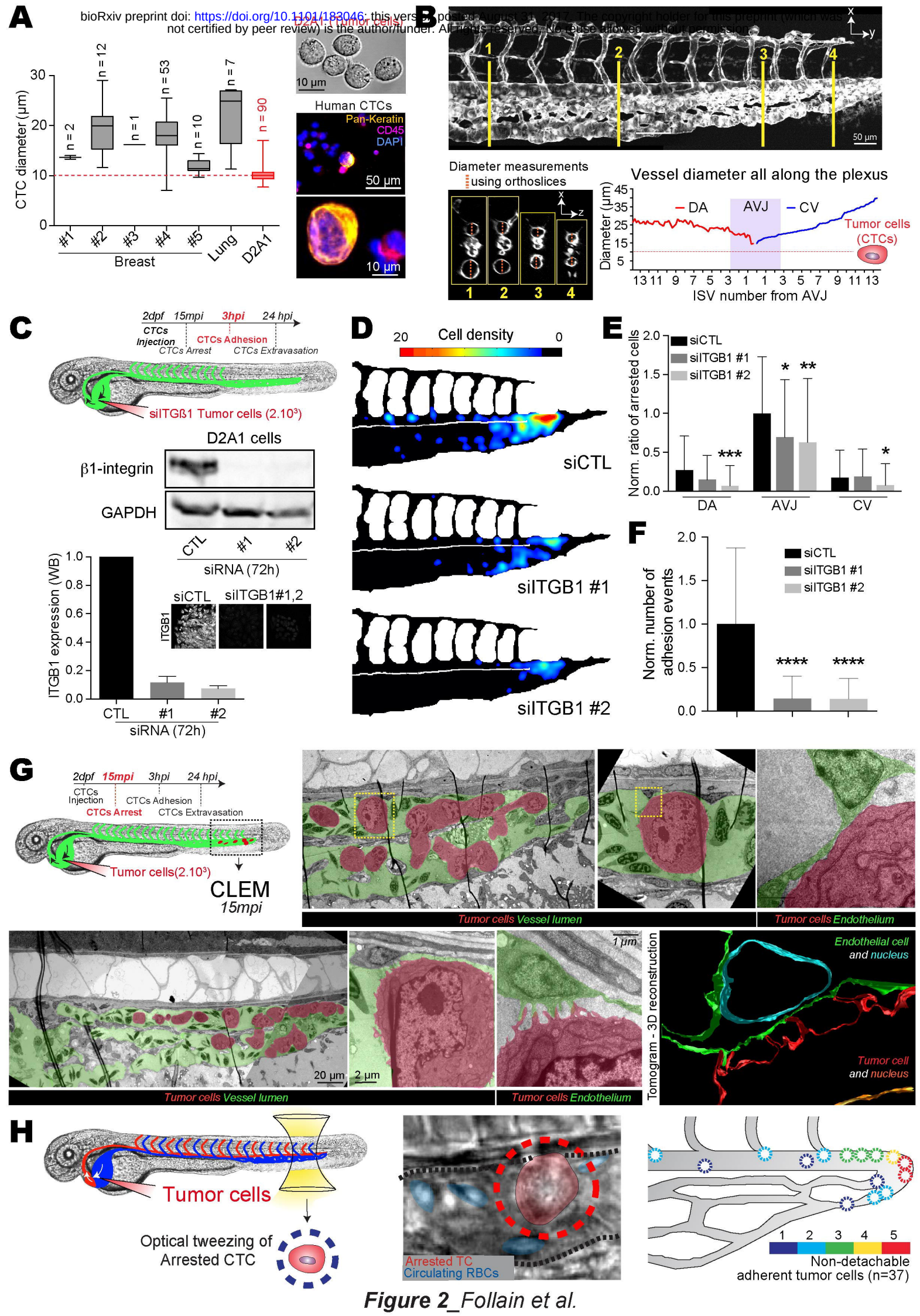

Figure 2_Follain et al.

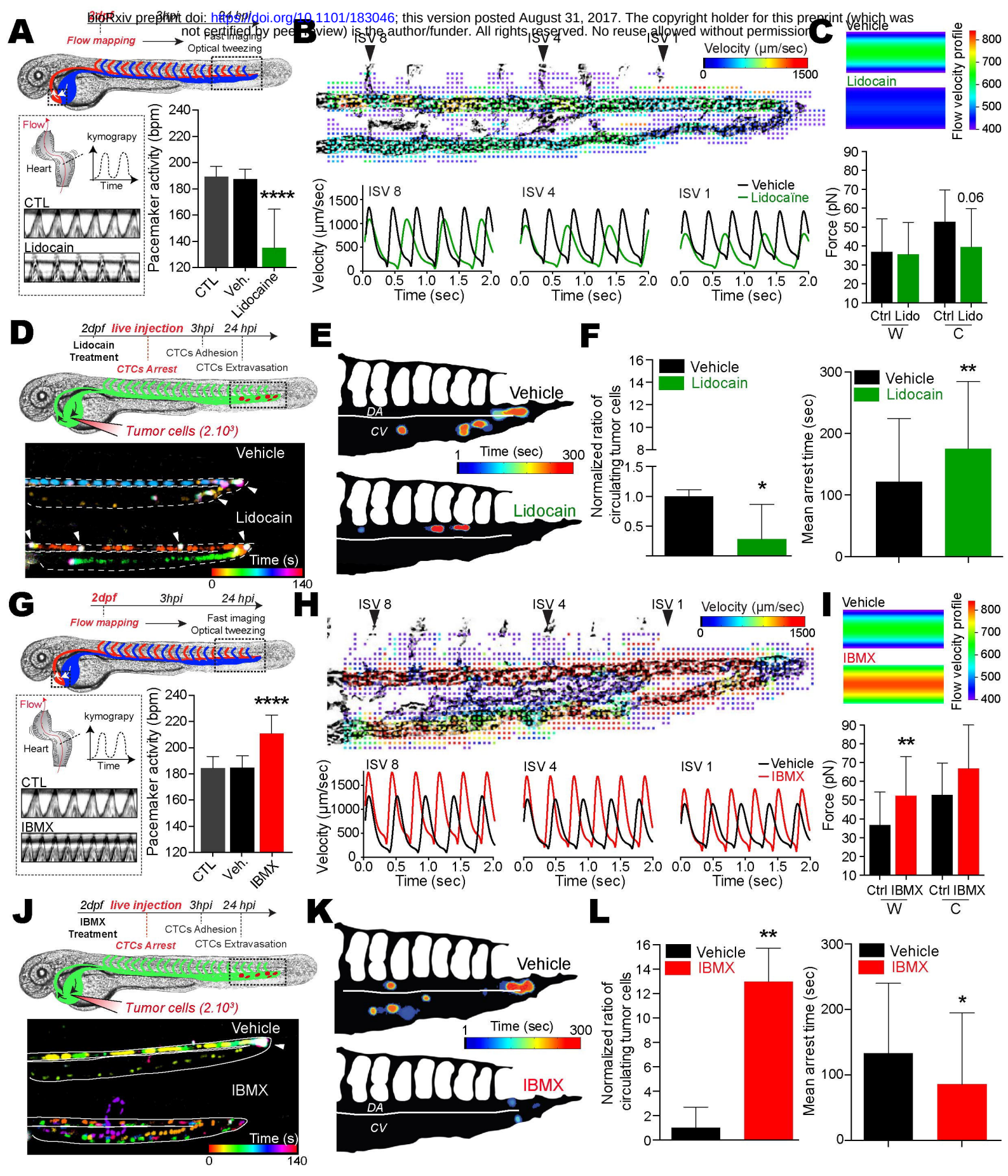

Figure 3_Follain et al.

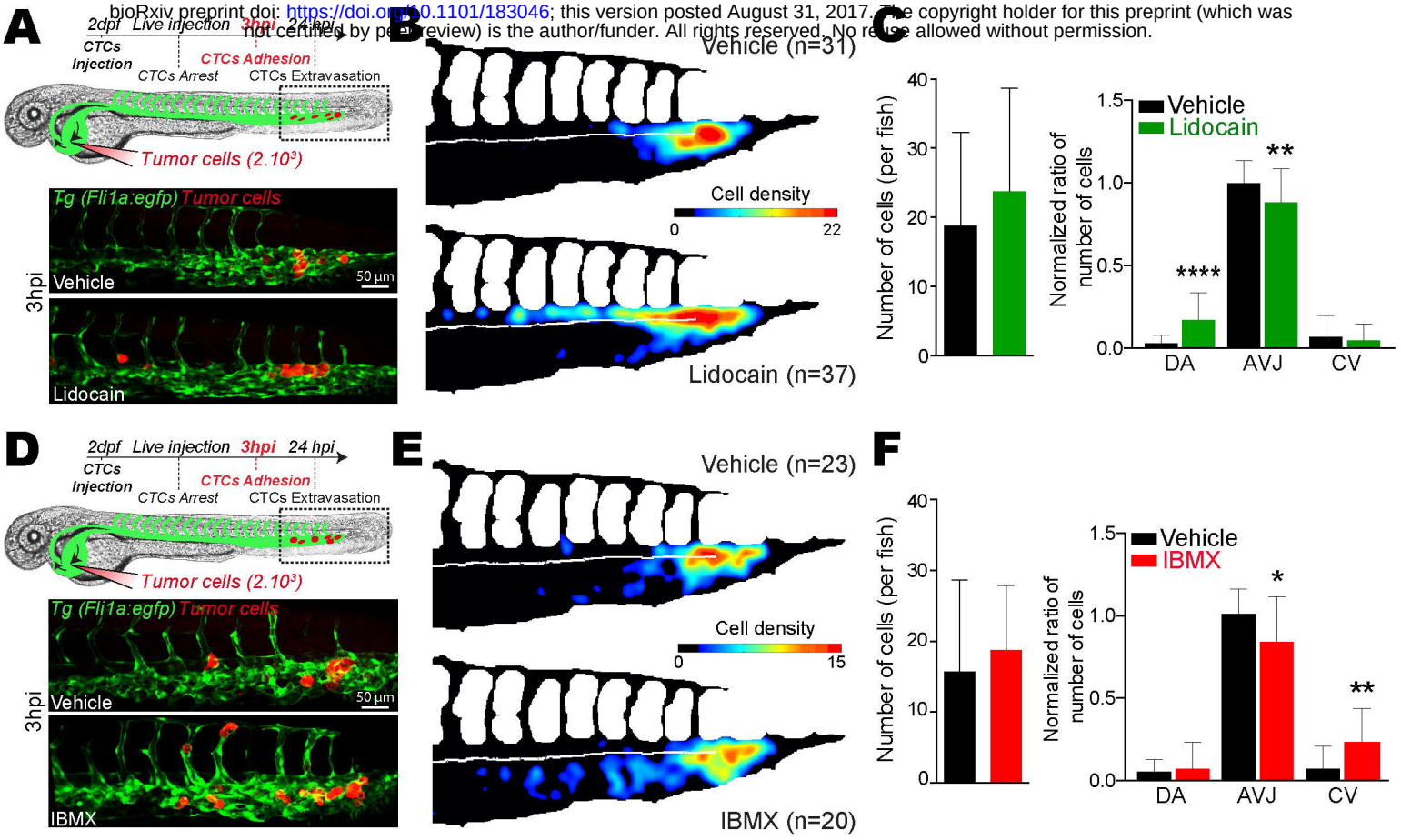

Figure 4_Follain et al.

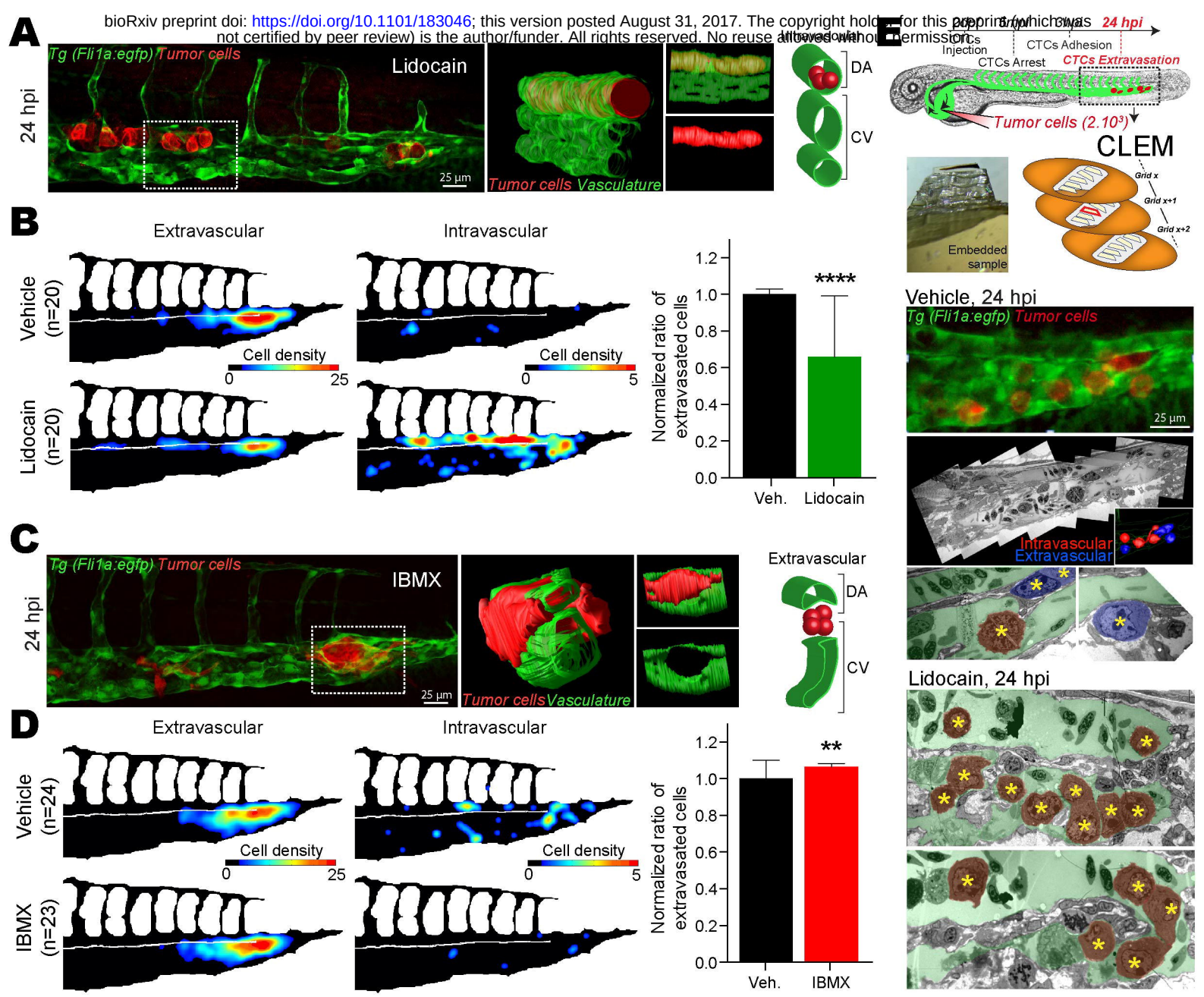

Figure 5_Follain et al.

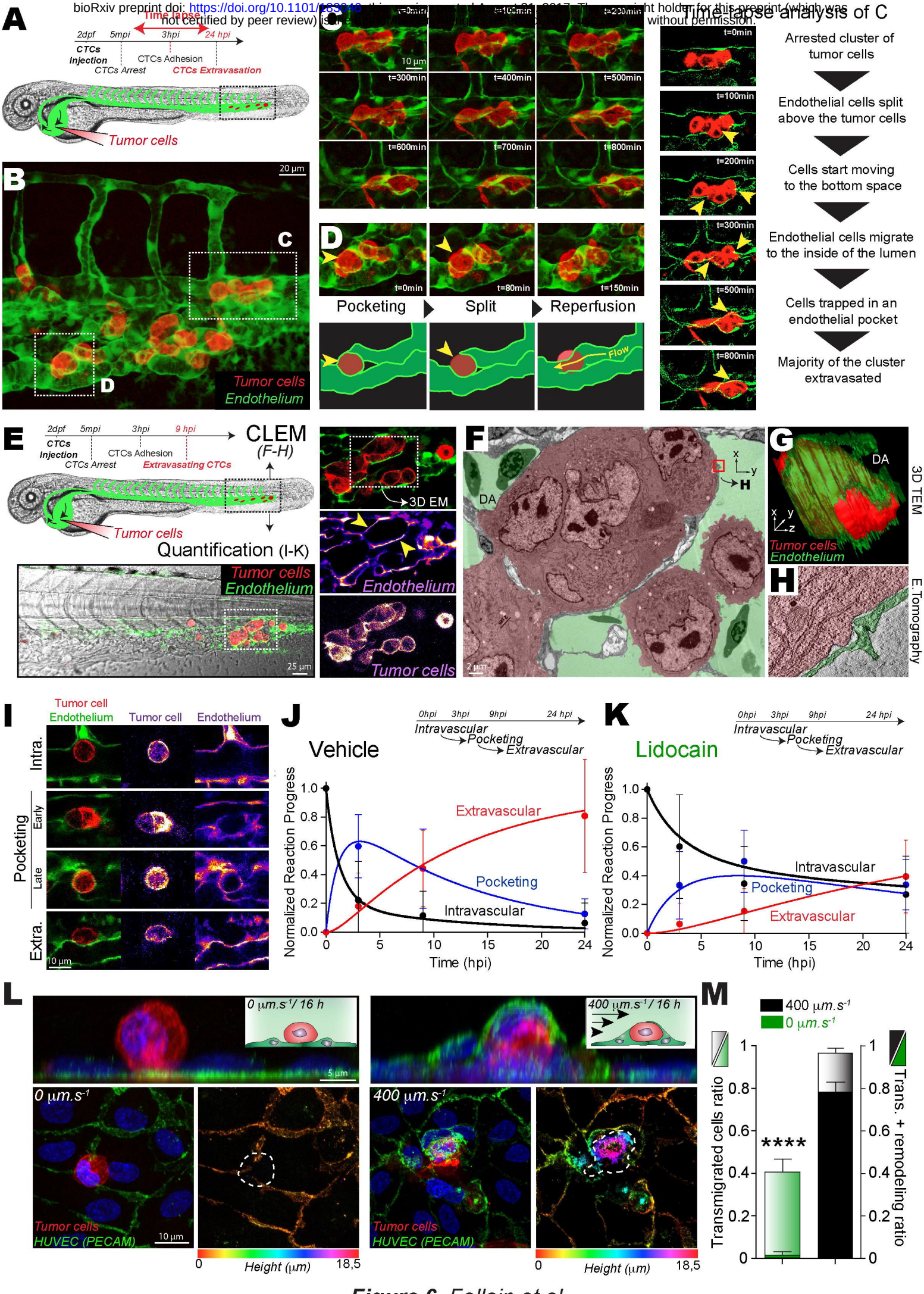

Figure 6_Follain et al.

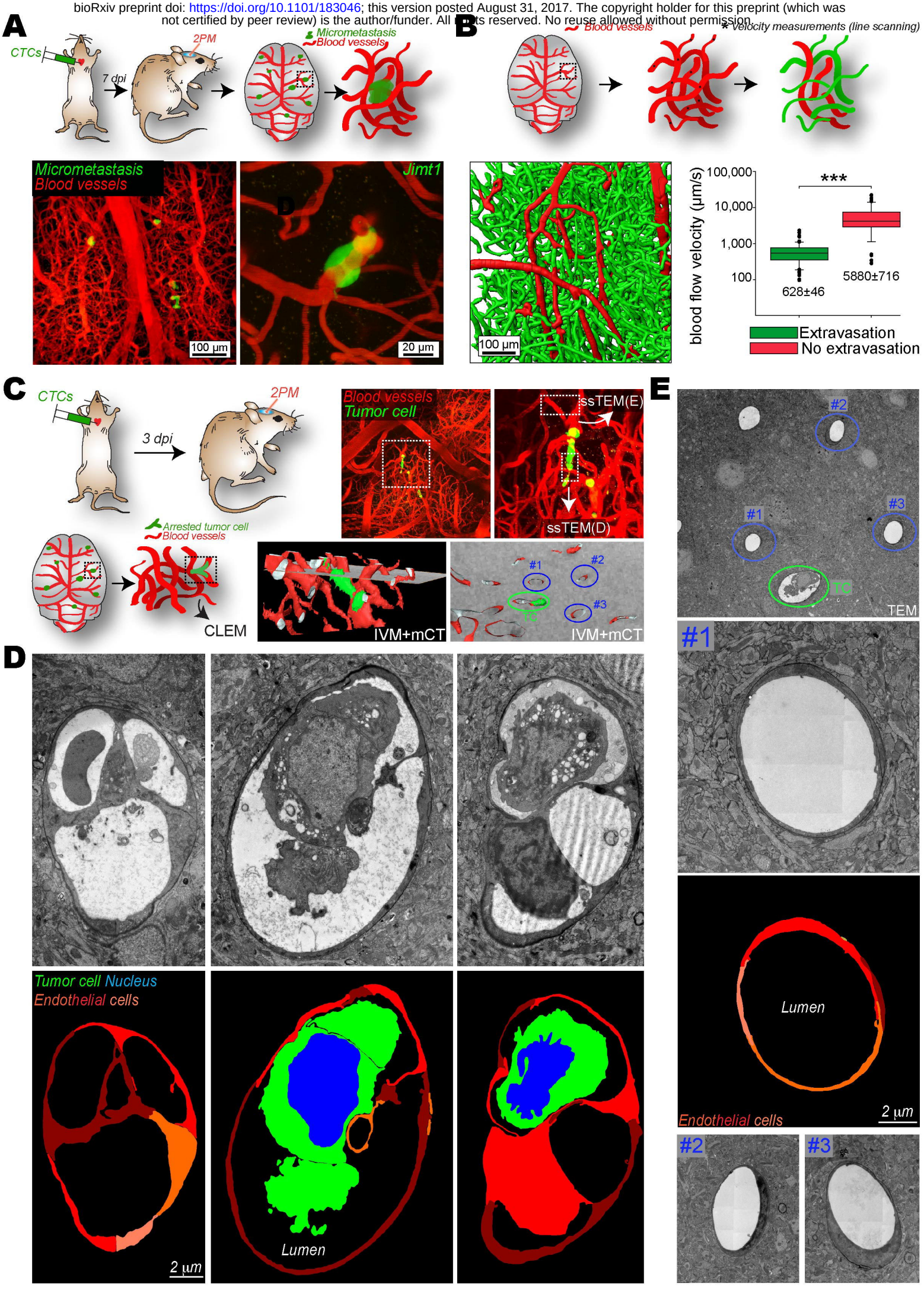

Figure 7_Follain et al.

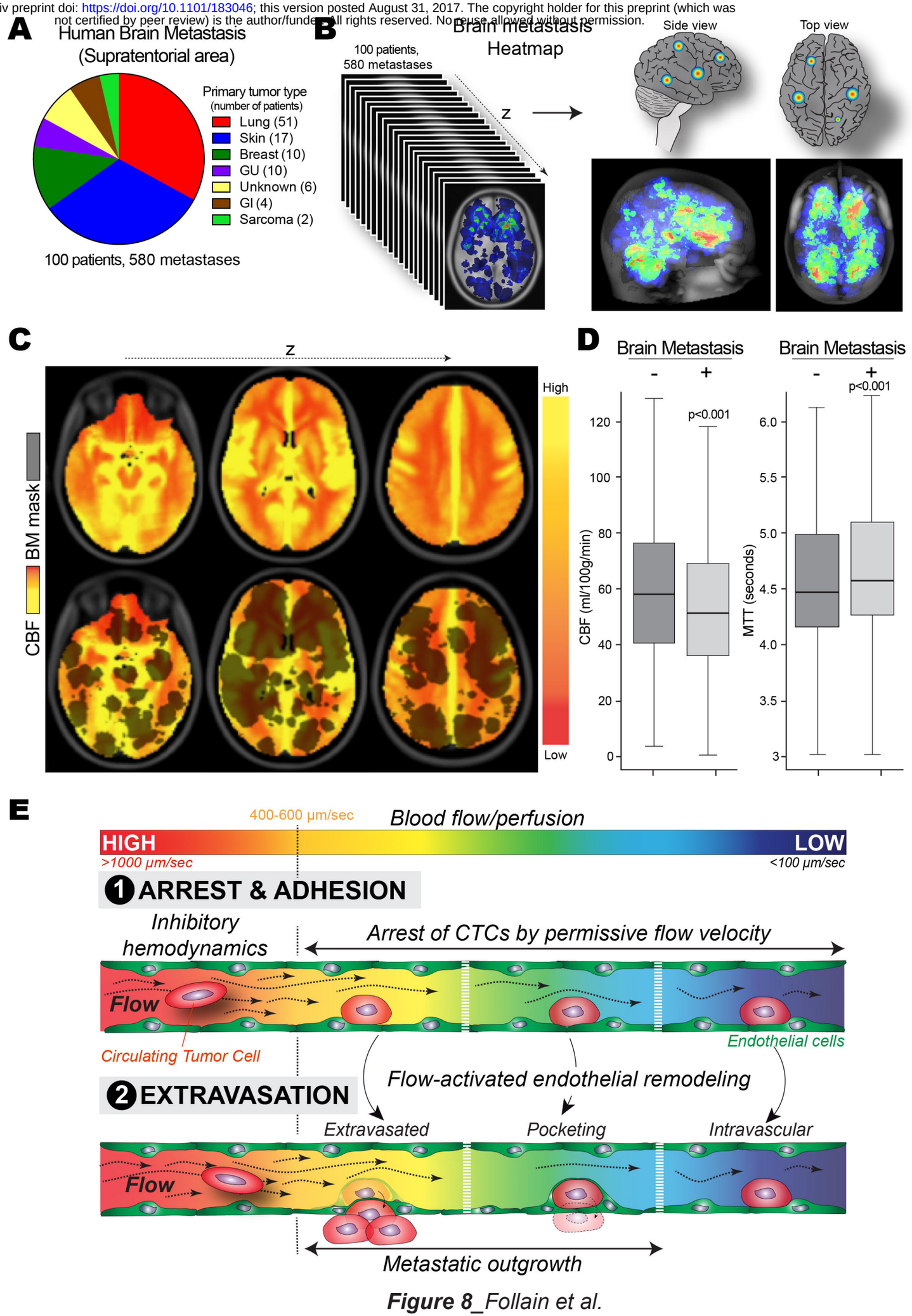

Figure 8_Follain et al.